Theoretical Study of Carrier Capture into Semiconductor Quantum Wells

PhD Thesis

Karol KÁLNA
Department of Theory of Semiconductor Microstructures
Institute of Electrical Engineering, Slovak Academy of Sciences
Dúbravská cesta 9, 842 39 Bratislava, Slovakia

Supervisor: RNDr. Martin MOŠKO, CSc.

Bratislava, October 1997

To Viki and Kajo

Contents

Preface

Miniaturization of electronic devices was fast progressing during the last twenty years. Very small devices not only work faster and consume less energy but also provide new functions and show new physical effects. Information revolution is in progress and a semiconductor laser is one of the leading components in information technologies.

To improve semiconductor lasers, a detailed knowledge of carrier dynamics is necessary. The purpose of this work is to theoretically investigate the carrier capture into semiconductor quantum wells, since this physical process plays an important role in so-called semiconductor quantum well lasers and is a subject of basic experimental studies via the time-resolved optical measurements. We would like to address the question how a detailed knowledge of the carrier capture mechanism may help to optimize the *GaAs* quantum well laser performance. Furthermore, we present a theoretical interpretation of previous time-resolved optical measurements of the carrier capture time.

The text is organized as follows: In Chapter 1, basic principles of semiconductor quantum well lasers are reviewed in order to point out the importance of the capture process in these devices. Previous time-resolved measurements of the capture process are briefly reviewed and experimental results open for theoretical interpretation are presented. Here also the goals of the thesis are specified. In Chapter 2, the author gives a semiclassical model of the hole capture time and a quantum-mechanical model for the electron capture time via the electron-polar optical phonon interaction. In Chapter 3 an ambipolar model which includes both these models interprets the experimental data. Most of the author's original contribution to the field is described in Chapter 4, where a quantum-mechanical model of the electron capture is presented in detail for the electron-electron (e-e) interaction without and with degeneracy and/or exchange effect, and for the electron-hole (e-h) interaction. The original author's contributions include: (i) derivation of the thermionic semiclassical hole capture time, (ii) incorporation of the degeneracy and exchange effect into the e-e capture time, (iii) derivation of the static screening function for the intersubband e-e interaction, and (iv) derivation of the intersubband e-h interaction where the static screening function contains a screening not only from electrons but also from holes. Numerical results and comments are given in Chapter 5. Finally, conclusions are presented in the Chapter 6.

Acknowledgments. I would like to thank my supervisor Dr. M. Moško for collaboration, help, careful leading of the work, and for many useful discussions. I acknowledge the help I received from my colleagues: Dr. M. Mošková, Dr. B. Olejníková, and P. Vagner. I wish to thank Prof. F. M. Peeters for his hospitality at the Department of Physics, University of Antwerp. This work would not be finished if I did not enjoy continuous support of my wife Gabriela.

Chapter 1

Introduction

1.1 Semiconductor Lasers

In this chapter we review basic principles of semiconductor lasers in order to point out the importance of the carrier capture process in so-called semiconductor quantum well (QW) lasers.

We can imagine the semiconductor laser as a two level system (see Fig. 1.1). If a photon with energy $\hbar\omega$ irradiates a two level system, a carrier from the lower energy level can pass into the upper one during the photon absorption. Then the carrier immediately falls back down into the lower energy level emitting a photon via the spontaneous emission. The principle of the laser activity is continuous photon emission which is called the *stimulated emission*. The stimulated emission in the semiconductor lasers is achieved via creation of *population inversion* at a *p-n* junction [2] under a forward bias (see Fig. 1.2).

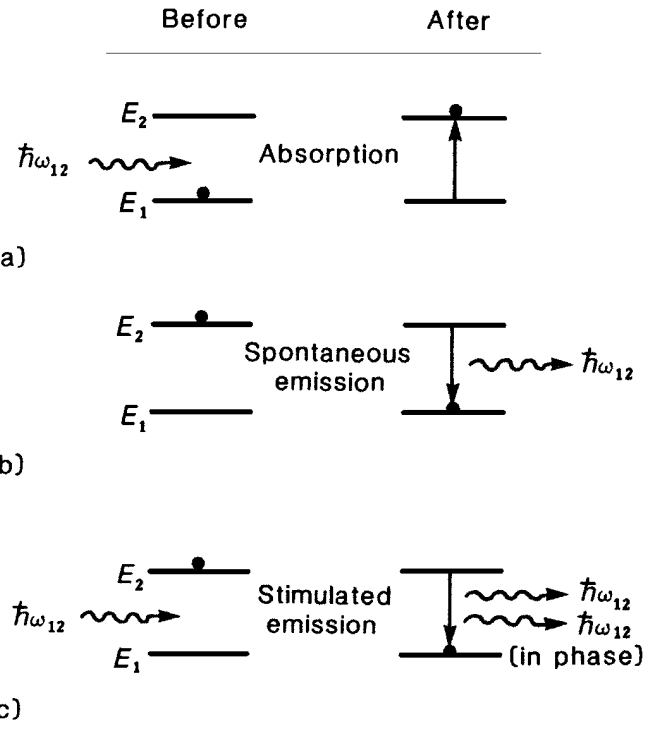

Figure 1.1: *The basic optical processes in a direct-gap semiconductor: (a) absorption, (b) spontaneous emission, and (c) stimulated emission of a photon. After Kelly [1].*

The population inversion takes place when a major part of electrons is at the upper energy level of the *p-n* junction and a minor part at the lower one. At the lower energy level, there is a major part of holes while the upper energy level contains only a minor

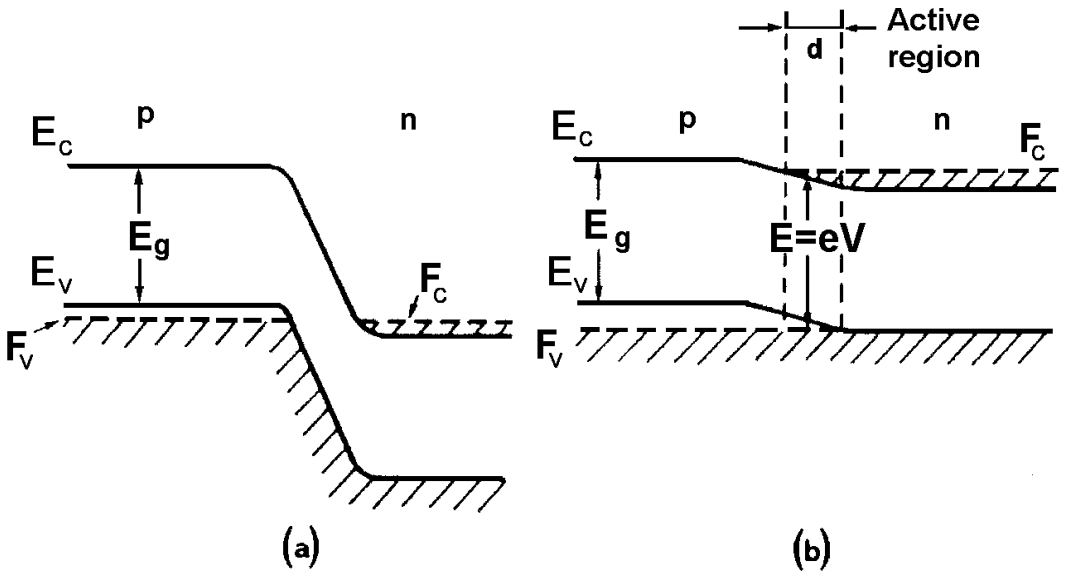

Figure 1.2: *Band diagram of a p-n junction semiconductor laser with (a) zero bias and (b) forward bias. After Svetlo [2].*

part [3]. An electron in the upper energy level is stimulated to fall to the lower one and to emit a photon in a much shorter time than its mean spontaneous decay time. The junction area where this behavior happens is called the *inversion region*. The population inversion must be retained during the whole laser activity in order to maintain a continuous stimulated emission in the inversion region (Another condition for the laser activity is the existence of a resonant optical cavity in which the emitted photons can be accumulated).

The population inversion at the *p-n* junction can be described with the help of quasi-Fermi levels. The population inversion exists usually between the bottom of the conduction band E_C and the top of the valence band E_V as it is drawn in Fig. 1.2. The proper transition levels are then in the conduction band up to the level F_C and in the valence band up to the level F_V. The carrier passing in the stimulated emission process from the conduction band into the valence band emits a photon with energy $h\nu$. For the energy $h\nu$ the population inversion exists when

$$F_C - F_V > h\nu \geq E_C - E_V. \tag{1.1}$$

The condition for the stimulated emission of a photon is given by [4]

$$E_C - E_V \equiv E_g = h\nu, \tag{1.2}$$

where E_g is the semiconductor bandgap. Dominant transitions for laser activity are determined by the resonant cavity and strong recombination near $h\nu = F_C - F_V$. The inequality (1.1) defines a range of the emitted photons and then even a laser spectrum.

The wavelength λ of the emitted photon is determined by the resonant cavity length L as

$$\lambda = \frac{2nL}{\mathsf{m}} \tag{1.3}$$

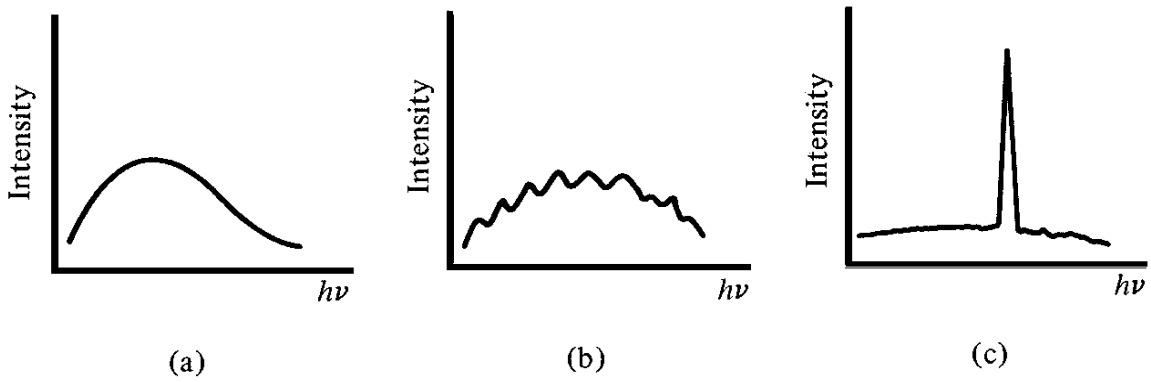

Figure 1.3: *Light intensity vs. photon energy hν for the p-n junction laser. (a) incoherent emission below threshold, (b) laser modes at threshold, and (c) dominant laser mode above threshold. The intensity scales are greatly compressed from (a) to (b) to (c). After Streetman [5].*

where m is an integer number and n is the refraction index.

Figure 1.3 illustrates the characteristic curves of emission intensity versus the photon energy for semiconductor lasers. At lower current levels (Fig. 1.3a) only the spontaneous emission occurs in the energetic range given by (1.1). With the current increased to the point where significant population inversion exists, stimulated emission begins together with the spontaneous emission which occurs at frequencies corresponding to cavity modes as shown in Fig. 1.3b. If the current level is high enough, the most preferred mode is dominating in the spectral output (Fig. 1.3c). This very intense mode represents the main laser output of the device.

The laser device with one *p-n* junction mentioned previously is a homojunction laser. More effective lasers can be obtained by using several layers in a laser structure. One of the layers in these heterojunction lasers is narrow enough to confine injected carriers and in this way creates the population inversion at lower threshold currents.

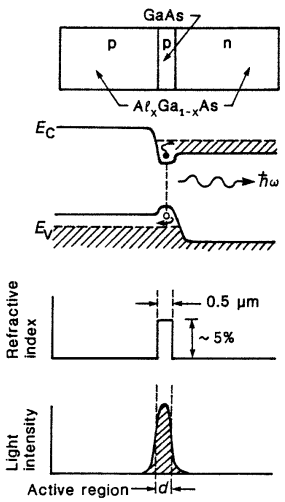

Figure 1.4: *Schematic sketch and band diagram of a double-heterojunction semiconductor laser. After Sze [6].*

The inversion region in *GaAs* lasers appears primarily on the *p*-side of the junction due to a higher efficiency of the electron injection than the hole injection. In a normal *p-n* junction the injected electrons diffuse into the *p* material such that the population inversion occurs only for a part of the electron distribution near the junction. However, if the *p* material is narrow and terminated in a barrier, the injected electrons can be confined near the junction as can be seen in Fig. 1.4. As

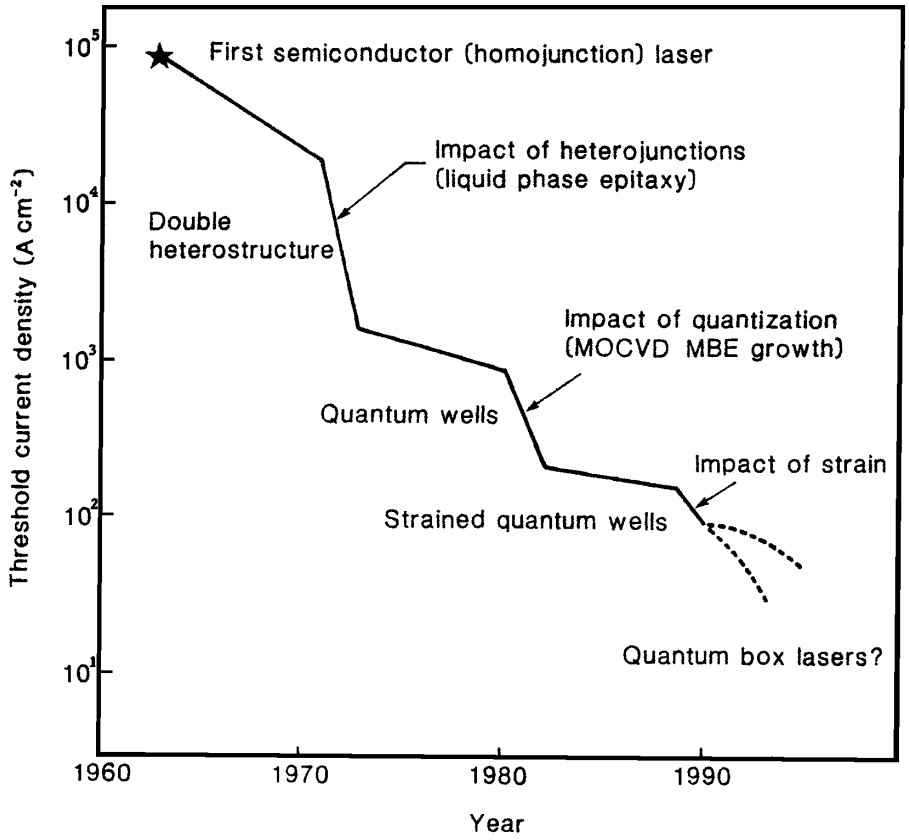

Figure 1.5: *The threshold current density of GaAs-based lasers. After Weisbuch and Nagle [8].*

a result, the laser action begins at a substantially lower current that for simple *p-n* junctions. In addition to the effects of the carrier confinement, the change of refractive index at the heterojunction provides a waveguide effect for the optical confinement of photons.

Further improvement can be achieved by sandwiching the active *GaAs* layer between two *AlGaAs* layers. This double-heterojunction structure further confines the injected carriers to the active region, and the change in refractive index at the *GaAs*/*AlGaAs* boundaries helps to confine the generated photons. The double-heterojunction laser is especially well suited to fiber optic communication systems [7].

Nowadays, the aim is to make increasingly efficient lasers and to reduce the level of current at the threshold of a laser operation [8]. Figure 1.5 points out the development of the threshold current density for *GaAs* lasers over last 20 years as new design principles have been incorporated.

The semiconductor QW laser is essentially a double-heterojunction semiconductor laser mentioned above, however, with a very narrow *GaAs* layer in order to achieve the quantum confinement of carriers. The QW laser has the kinetic energy of the carriers quantized into

discrete energy levels similar to the quantum mechanical problem of the 1D potential well. The QW laser has the possibility to change the emission wavelength by varying the QW width.

Confined carriers must have a high enough density in the QW, so that the recombination can proceed continuously in the active region. The supplement of carriers in the QW is facilitated from cladding layers during the so-called *capture process*. The time of the carrier transition from the state above the barrier into a bound state in the QW is a *capture time*. The shorter the capture time the faster the creation of the population inversion, and the laser works at a lower threshold current and/or with better high-speed modulation characteristics [9].

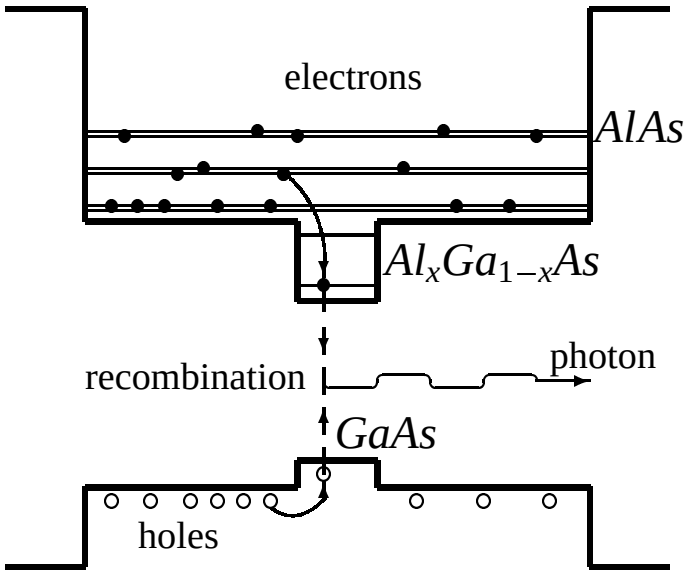

Figure 1.6: *Carrier capture processes from the conduction and valence bands are depicted schematically in a separate confinement heterostructure quantum well.*

Figure 1.6 shows the QW laser structure which has additional barriers. The purpose of these barriers is to collect the carriers near the QW in order to increase their capture efficiency into the QW. Then the QW laser can achieve the population inversion in the QW at a lower threshold current. Note here that the *AlAs* cladding layers create also optical confinement [10]. Throughout this work the capture time in the structure shown in Fig. 1.6 will be analyzed.

1.2 Measurements of Carrier Capture Time

Measurements of carrier capture dynamics in the semiconductor QW laser structures (Fig. 1.6) are provided by time-resolved optical experiments [11, 12]. From experimental point of view, there are two regions, the barrier and well, each with a distinct bandgap which serve as two different optical markers [13]. The time evolution of these two spectra provides information about the electron and hole capture into the QW.

The following experimental methods are used: (i) *upconversion spectroscopy* and (ii) *pump-probe spectroscopy*. For both experimental techniques the time resolution is limited only by the duration of a laser pulse [12].

In the upconversion technique [14] the capture times are determined from differences in the rise time of the QW luminescence after direct (below the *AlGaAs* barrier band gap) and indirect (above the *AlGaAs* barrier band gap) excitation with a subpicosecond laser pulse (see Fig. 1.7), in order to eliminate the effect of carrier relaxation in the QW. The difference of these two excitation energies, direct and indirect, is equal to the LO-phonon energy. To have the same

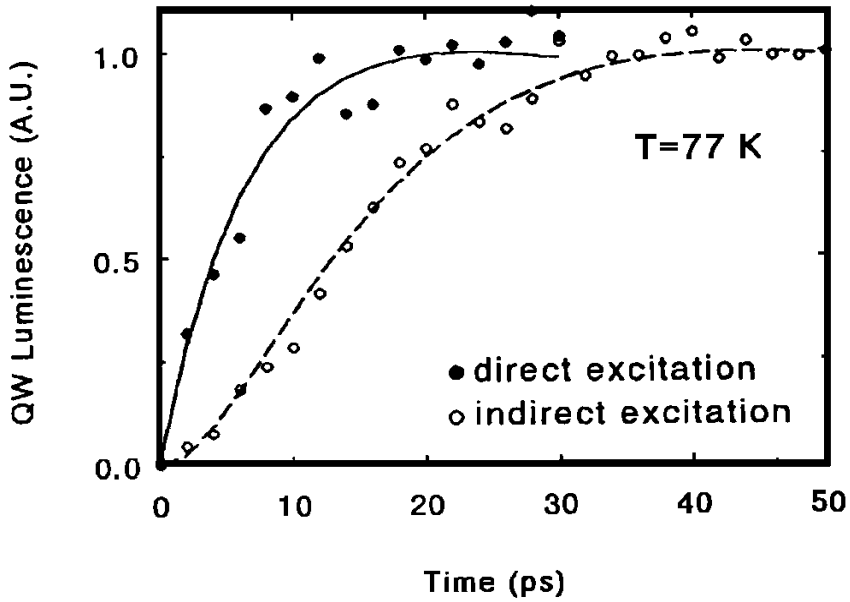

Figure 1.7: *Experimental determination of the carrier capture time using the upconversion technique. After Blom [11, 12].*

cooling inside the QW for direct and indirect excitation, the number of carriers inside the well is kept constant in both cases.

In the pump-probe technique the capture time is determined from the decay of a barrier population in two-pulse correlation measurements [15]. A strong excitation pulse creates electrons and holes in the *AlGaAs* barrier states (see Fig. 1.6) and thus reduces the absorption of the second laser pulse with the same photon energy. If the delay between the laser pulses exceeds the carrier capture time, then the absorption of the second laser pulse is no longer reduced. The barrier correlated luminescence is expected to increase with increasing time delay between the laser pulses until the carriers of the first laser pulse are captured in the QW (see Fig 1.8a). In Fig. 1.8b is shown a further possibility which looks at the correlated luminescence of the *GaAs* buffer layers. This luminescence decreases with increasing time delay until the carriers are captured.

Figure 1.9 shows the carrier capture time versus the QW width, extracted from the upconversion and pump-probe experiments [11, 12]. The measured carrier capture time oscillates as a function of the QW width and these oscillations are reproduced by the calculated ambipolar capture time. The origin of the oscillations will be discussed in detail in Chap. 5, here only a basic information is given in order to define open problems. The ambipolar capture time is the average of the electron and hole capture rates [Eq. (2.2) in Chap. 2]. The calculations of the ambipolar capture time in Fig. 1.9 include the quantum-mechanical calculation of the electron capture due to the polar optical phonon emission and the classical diffusion model of the hole capture which gives a constant (QW-width independent) hole capture time. The oscillations are thus due to the electron capture and their origin is purely quantum-mechanical. They were predicted for the first time in Refs. 16 and 17, where it was pointed out that the overlap of the

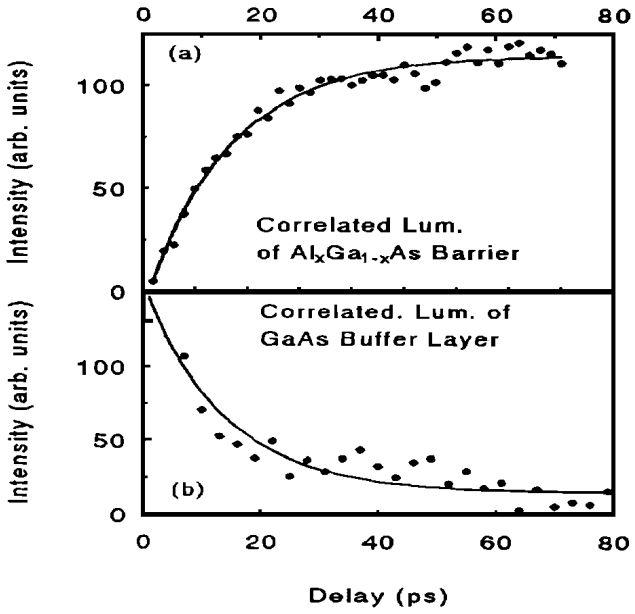

Figure 1.8: *Experimental determination of the carrier capture time using the pump-probe technique. In the upper part (a) the correlated AlGaAs barrier luminescence is plotted as a function of the time delay between two laser pulses. In the lower part (b) the correlated luminescence of the GaAs buffer layer, which is located below the QW structure, is also plotted as a function of the delay. After Blom [11, 12].*

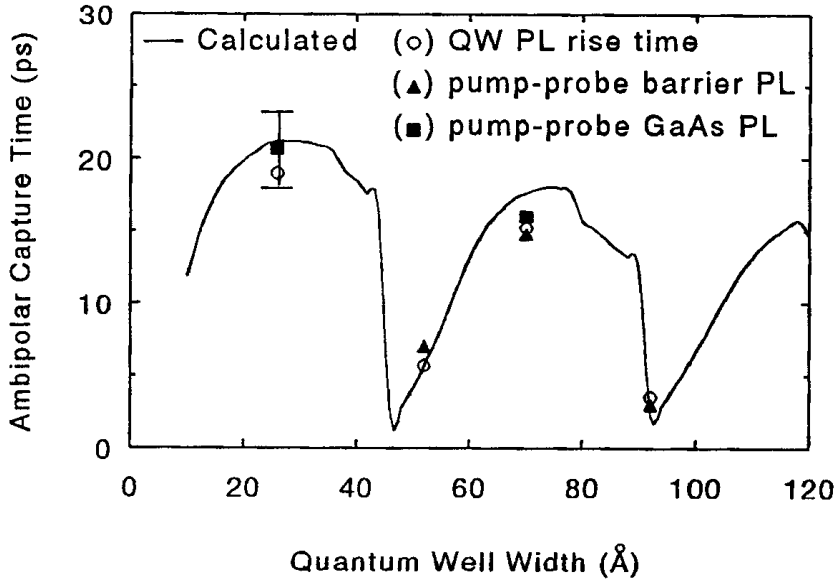

Figure 1.9: *Observation of an oscillating carrier capture time is compared with the calculated ambipolar capture time. The experimental data were obtained from the upconversion measurement (open circles), the two-pulse correlation measurements (full triangles), and the "transmission-like" correlation experiments. After Blom [11, 12].*

electron envelope functions of the energy levels above and below the *AlGaAs* barrier, which determines the strength of the capture, oscillates as a function of the QW width.

Despite the good quantitative agreement of the measured and calculated capture times in Fig. 1.9, there is a number of open problems in the carrier capture theory. Those addressed in this work can be summarized as follows:

1. As will be shown later on (Chap. 3), the hole capture cannot be viewed as a classical diffusion process and using of the constant hole capture time in the calculations of Fig. 1.9 is not justified. In the light of this finding the agreement between the calculation and experiment in Fig. 1.9 is fortuitous and obscures the open problem of the hole capture treatment beyond the diffusion model.

2. The above discussed measurements give the same capture time results in a broad range of photoexcited carrier densities ($2 \times 10^{15}\text{cm}^{-3} - 10^{17}\text{cm}^{-3}$), which strongly suggests that the carrier-carrier (c-c) scattering induced capture plays a minor role compared to the considered optic phonon emission induced capture. However, in laser applications, much higher carrier densities than 10^{17}cm^{-3} are injected into the QW structure of Fig. 1.6 and the c-c scattering might be important. Therefore, a detailed analysis of the c-c scattering induced capture is needed in conditions which are characteristic for the laser action.

3. In Ref. 18 it was theoretically predicted that the electron-electron (e-e) scattering induced capture is even more efficient than the phonon emission induced capture. This prediction contradicts the experiment, because the carrier densities considered in the calculations of Ref. 18 are close to the densities in the (above discussed) measurements confirming a minor role of the c-c scattering. Thus, another motivation for the analysis of the c-c scattering induced capture is to remove this contradiction.

1.3 Goals of Doctoral Thesis

With regards to the open problems discussed in previous sections we formulate the following thesis goals:

1. To estimate the hole capture time into the *GaAs* QW from a proper semiclassical model.
2. To calculate the electron-polar optical phonon (e-pop) interaction induced capture time into the *GaAs* QW.
3. To calculate the ambipolar capture time and to compare our theoretical results with the capture times measured in time-resolved optical experiments [11].
4. To understand the role of the e-e scattering in the electron capture process for various QW parameters (QW width, carrier density, etc.).
5. To incorporate the degeneracy and exchange effect (particle indistinguishability) into the e-e capture in order to make the analysis more reliable.
6. To assess the time for the electron capture via the electron-heavy hole (e-h) scattering (the capture process mostly ignored).
7. Finally, to point out how the QW laser structure can be optimized on the basis of the calculated carrier capture times.

Chapter 2

Classical and Quantum-Mechanical Models of Carrier Capture into Quantum Well

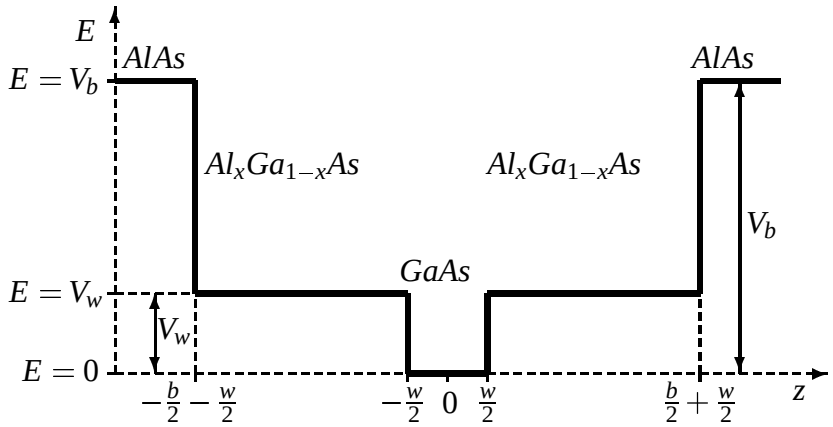

Figure 2.1: *Potential shape of the separate confinement heterostructure quantum well.*

The separate confinement heterostructure quantum well (SCHQW) is an experimental structure for an investigation of the capture processes in the QW laser. The analyzed SCHQW consists of the *GaAs* QW with width which varies from 10 to 124 Å, embedded between the two 500 Å $Al_xGa_{1-x}As$ barriers. Whole structure is covered by semiinfinite *AlAs* layers as shown in Fig. 2.1. The QW width is denoted as w and the barrier width as $b/2$. The temperature of 8 K is considered. The same structure was investigated in previous work [11, 18–21], since it is of interest for the optical measurements of the capture time as well as for the laser applications.

There are two main approaches how to characterize theoretically the carrier capture process: (i) the classical fluid model and (ii) the quantum-mechanical model. The validity of the quantum-mechanical model based on the *Fermi Golden Rule* depends on a coherence length of carriers and the coherence length is limited with inelastic scattering processes. If the coherence length of the carriers is less than the total width of the structure ($b+w$; see Fig. 2.1), then the carriers are not able to create a coherent wave function and should be described as a classical fluid.

The most general approach which takes into account the loss of the phase coherence in the carrier wave functions due to the strong inelastic scattering is the simulation of the carrier capture in the QW through the so-called Schrödinger equation Monte Carlo method [22–24].

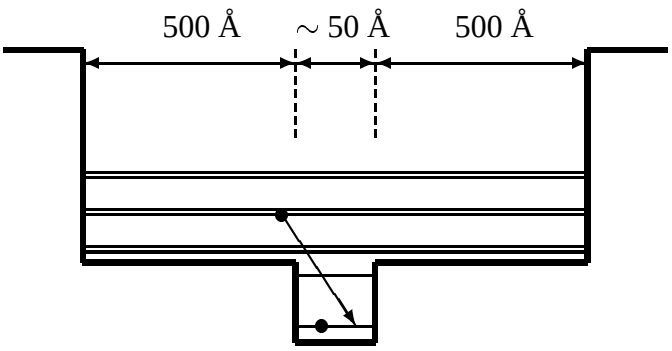

Figure 2.2: *Schematic view of the capture process into the QW in SCHQW.*

Because the electron coherence length exceeds the width of the structure but the hole coherence length is smaller [11], we intend to calculate the electron capture time using the quantum-mechanical model, and the hole capture time by using the semiclassical model. Figure 2.2 depicts a capture transition of an electron from an energy level on the barrier into a bound state in the QW.

At low excess energies holes are captured first due to their greater effective mass. After the hole capture into the QW, the holes electrostatically attract electrons into the QW and so increase the electron capture rate. The remaining holes in the barrier will be electrostatically repulsed from the QW and thus decrease the hole capture rate. The net result is the ambipolar capture process with a capture rate between the capture rates of the electrons and holes. To account for the ambipolar process in a simple form, the electron capture time τ_e and the hole capture time τ_h are usually set into a rate equation model [12]

$$\begin{aligned} \frac{dn_e}{dt} &= -\frac{n_e}{\tau_e} - \frac{1}{2}\left(\frac{n_h}{\tau_h} - \frac{n_e}{\tau_e}\right) \\ \frac{dn_h}{dt} &= -\frac{n_h}{\tau_h} + \frac{1}{2}\left(\frac{n_h}{\tau_h} - \frac{n_e}{\tau_e}\right), \end{aligned} \tag{2.1}$$

and the electron density in the barrier, n_e, is assumed to be equal to the hole density in the barrier, n_h. Then the ambipolar capture time τ_a can be defined as [19, 25]

$$\frac{1}{\tau_a} = \frac{1}{2}\left(\frac{1}{\tau_e} + \frac{1}{\tau_h}\right). \tag{2.2}$$

2.1 Semiclassical Model of Hole Capture

In the following we develop a semiclassical model of the heavy hole capture time. Under the collision-free hole transport conditions, the thermionic emission current fills the QW [26]. Then one can estimate the thermionic capture time for a hole using the Bethe relation [6] as

$$\tau_{\text{therm}} = \frac{b}{2}\left(\frac{\pi m_h^B}{2E_h^B}\right)^{1/2} \exp\left(\frac{e\Phi}{k_B T}\right), \tag{2.3}$$

where m_h^B is the heavy hole effective mass and E_h^B is the hole energy, both in the *AlGaAs* barrier.

$e\Phi$ in Eq. (2.3) represents the potential wall for the hole in the *AlGaAs*, created by the space charge. This potential can be estimated from the Poisson equation assuming the spatially independent densities for electrons and holes on the *AlGaAs* barriers. One gets

$$\Phi = \frac{e}{2\kappa^B}(n_e - n_h)\left(\frac{b}{2}\right)^2, \tag{2.4}$$

where κ^B is the static permittivity of the *AlGaAs* barrier.

Now we wish to argue that in the experiments of interest the barrier $e\Phi$ was negligibly small. Experimental measurements [11] show that there is no dependence of the capture time on an excitation density in the range from 3×10^{15} to $2\times10^{17}\mathrm{cm}^{-3}$. These results were obtained for undoped SCHQW structures as well as for the SCHQW structures with *n*-doped and *p*-doped QWs. The absence of density dependence of the carrier capture time in such a broad range of carrier densities strongly suggests that $\exp\left[e\Phi/(k_BT)\right] \approx 1$. We can then estimate from (2.4) that the space charge density in the *AlGaAs* barrier, $n_e - n_h$, is smaller than $2.5\times10^{14}\mathrm{cm}^{-3}$. This can be qualitatively understood as follows: Certain number of holes remains in the barrier because they are electrostatically repulsed by holes captured in the QW. In the same time, the electron density decreases owing to the electron attraction by the holes captured in the QW. As a consequence of this ambipolar process, the electron and hole densities in the barrier tend to remain the same. Thus Eq. (2.3) can be reduced to a simple relation

$$\tau_{\mathrm{therm}} = \frac{b}{2}\left(\frac{\pi m_h^B}{2E_h^B}\right)^{1/2}. \tag{2.5}$$

If the hole mean free path due to the polar optical phonon emission, ℓ, is greater than the *GaAs* QW width *w*, the hole capture rate should be reduced by the probability $[1-\exp(-w/\ell)]$ that the hole emits optical phonon when crossing the QW:

$$\frac{1}{\tau_h} = \frac{1}{\tau_{\mathrm{therm}}}\left(1 - e^{-\frac{w}{\ell}}\right). \tag{2.6}$$

If we assume that the hole is moving in the barrier as a classical particle, then the phonon emission probability in the QW is

$$1 - e^{-\frac{w}{\ell}} = 1 - \exp\left(-\frac{w}{\tau_{h-p}(E_h)\, v_h^W}\right), \tag{2.7}$$

where v_h^W is the z-component of the hole velocity above the QW.

The hole scattering time due to the optical phonon (h-p) emission reads

$$\frac{1}{\tau_{h-p}(E_h)} = \frac{1}{\tau_{h-pop}(E_h)} + \frac{1}{\tau_{h-nop}(E_h)}, \tag{2.8}$$

where

$$E_h = E_{\mathrm{excess}}\frac{m_e}{m_e + m_h} + V_w^h, \tag{2.9}$$

is the kinetic energy of the hole crossing the QW, E_{excess} is the laser excess energy, V_w^h is the depth of the QW in the valence band, and m_e and m_h are the electron and heavy hole effective masses in the QW, respectively.

The first term on the right-hand side of Eq. (2.8) is the emission rate via the heavy hole-polar optical phonon (h-pop) interaction which has the form [27, 28]

$$\frac{1}{\tau_{h-pop}(E_h)} = \sqrt{m_h/2}\,\frac{e^2\omega_{LO}}{4\pi\hbar}\left(\frac{1}{\kappa_\infty}-\frac{1}{\kappa}\right)\frac{1}{\sqrt{E_h}}\ln\left|\frac{\sqrt{E_h}+\sqrt{E_h-\hbar\omega_{LO}}}{\sqrt{E_h}-\sqrt{E_h-\hbar\omega_{LO}}}\right|, \tag{2.10}$$

where ω_{LO} is the frequency of longitudinal optical phonons, κ and κ_∞ are the static and high frequency permittivities, respectively, in the QW. The second term represents the heavy hole-nonpolar optical phonon (h-nop) emission rate in the form [29]

$$\frac{1}{\tau_{h-nop}(E_h)} = \frac{(2m_h)^{3/2}D_0^2}{4\pi\hbar^3\rho\,\omega_0}\sqrt{E_h-\hbar\omega_0}, \tag{2.11}$$

where D_0 is the nonpolar optic deformation potential, ρ is the mass density, v_L is the velocity of sound, and ω_0 is the nonpolar optic phonon frequency (see Table 5.1, p 38 for material parameters used in the calculations).

In Eq. (2.7) the z-component of the hole velocity can be found from the laser excess energy as

$$v_h^W = \sqrt{\frac{2}{m_h}\left(\frac{1}{3}E_{\text{excess}}\frac{m_e}{m_e+m_h}+V_w^h\right)}.$$

The model (2.5)-(2.7) can be further improved if we take into account that the carrier can be quantum-mechanically reflected at the edges of the QW (at points $-w/2$ and $w/2$; Fig. 2.1). Then

$$\frac{1}{\tau_h} = \frac{2}{b}\left[\frac{2E_{\text{excess}}}{3\pi(m_e^B+m_h^B)}\frac{m_e^B}{m_h^B}\right]^{1/2} T_{B\to W}\left[1-\exp\left(-\frac{w}{\tau_{h-p}\,(E_h)\,v_h^W\,T_{W\to B}}\right)\right], \tag{2.12}$$

where the transmission coefficient from the *AlGaAs* barrier into the QW is defined as [30]

$$T_{B\to W}\,(E_h-V_w^h) = \frac{4\sqrt{m_h^B m_h(E_h-V_w^h)E_h}}{\left(\sqrt{m_h^B(E_h-V_w^h)}+\sqrt{m_h E_h}\right)^2},$$

the transmission coefficient from the QW into the *AlGaAs* barrier as

$$T_{W\to B}\,(E_h) = T_{B\to W}\,(E_h-V_w^h), \tag{2.13}$$

and m_e^B is the electron effective mass in the barrier.

2.2 Quantum-Mechanical Model of Electron Capture via Interaction with Optical Phonons

In the following we deal with the e-pop interaction induced capture rate. If an electron with wave vector $\mathbf{k}_1$ is scattered on the polar optical phonon then the e-pop scattering rate from the subband i to the subband m for a spontaneous phonon emission reads [31, 32]

$$\lambda_{im}^{epop}(\mathbf{k}_1) = \frac{e^2\omega_{LO}m_e}{8\pi\hbar^2}\left(\frac{1}{\kappa_\infty}-\frac{1}{\kappa}\right)\int_0^{2\pi} d\theta\,\frac{F_{iimm}^{ee}(q)}{q\,\varepsilon^e(q)}, \tag{2.14}$$

where $\varepsilon^e(q)$ is the static two-dimensional screening function given by

$$\varepsilon^e(q) = 1+(q_S^e/q)F_{1111}^{ee}(q), \tag{2.15}$$

$$q = \left[2k_1^2+\frac{2m_e}{\hbar^2}E_S^e-2k_1\left(k_1^2+\frac{2m_e}{\hbar^2}E_S^e\right)^{1/2}\cos\theta\right]^{1/2}, \tag{2.16}$$

with $q_s^e = e^2m_e/(2\pi\kappa\hbar^2)\,f_1^e(\mathbf{k}_2=0)$ and $E_S^e = E_i^e - E_m^e - \hbar\omega_{LO}$.

A key role in the formula (2.14) plays the form factor

$$F_{iimm}^{ee}(q) = \int_{-\infty}^{\infty} dz_1 \int_{-\infty}^{\infty} dz_2\,\chi_i^e(z_1)\,\chi_i^e(z_2)\,e^{-q|z_1-z_2|}\,\chi_m^e(z_1)\,\chi_m^e(z_2), \tag{2.17}$$

where the electron wave function χ_γ^e in the subband γ ($\gamma = i,m$) is obtained assuming the x-dependent electron effective mass and the flat Γ-band with parabolic energy dispersion, both properly interpolated between *GaAs* and *AlAs* [33].

The electron capture time via the e-pop interaction for an optical experiment is a sum of the averaged individual capture transitions:

$$\tau_{e-pop}^{-1} = \sum_{i,m,\mathbf{k}_1}\frac{f_i^e(\mathbf{k}_1)\,\lambda_{im}^{epop}(\mathbf{k}_1)}{f_i^e(\mathbf{k}_1)}, \tag{2.18}$$

where the summation over i (m) includes only the electron subbands above (below) the *AlGaAs* barrier.

The optical matrix element in the absorption coefficient is proportional to [34, 35]

$$\int_{-\infty}^{\infty} dz_1\,\chi_i^e(z_1)\,\chi_j^h(z_1)\begin{cases}\approx 1 & \text{if} \quad i=j,\\ \approx 0 & \text{if} \quad i\neq j.\end{cases} \tag{2.19}$$

This selection rule implies that

$$N_i^e = N_j^e = N_i^h = N_j^h,$$

e.g., electron ($N_{i,j}^e$) and hole ($N_{i,j}^h$) sheet densities are equal in each subband. It also implies that the same number of electron and hole subbands is occupied after the excitation.

The form of the electron distribution function in the barrier (initial states) does not affect the electron capture time if the laser excess energy is larger than the polar optical phonon energy. When we assume that the carriers in the barrier are thermalized after an excitation by a short laser pulse then the distribution function $f_i^e(\mathbf{k}_1)$ can be taken as a Boltzmann distribution function in the form

$$f_i^e(\mathbf{k}_1) = \frac{\exp \frac{\varepsilon(\mathbf{k}_1)}{k_B T_i^e}}{k_B T_i^e}, \tag{2.20}$$

where the electron temperature T_i^e can be found from the relation

$$k_B T_i^e = \frac{m_h^B}{m_e^B + m_h^B}(E_{\text{excess}} - E_i^e - E_i^h). \tag{2.21}$$

In the relation (2.21), E_i^e and E_i^h are the initial electron and hole energies in the subband i, respectively.

On the other hand, we can assume that the carriers have not enough time to thermalize in the barrier before they are captured. Then, instead of the function (2.20), we can used the delta function distribution

$$f_i^e(\mathbf{k}_1) = \delta\left(\frac{\hbar^2 k_1^2}{2m_e^B} - k_B T_i^e\right). \tag{2.22}$$

To determine whether the carriers are thermalized or not, the calculated capture time will be compared with the measured one as a function of the laser excess energy (see Chap. 3).

Chapter 3

Interpretation of Experiment

The time-resolved optical measurements of the carrier capture time in the SCHQWs were described in Sec. 1.2. The carrier capture is an ambipolar process, which means that the measured capture time has to be compared with the ambipolar capture time (2.2). As already discussed in Sec. 2.2, the electron capture time entering the ambipolar expression (2.2) can be evaluated from the formulae (2.14-2.18) with a properly chosen electron distribution function $f_i^e(\mathbf{k}_1)$. The problem is how to evaluate the hole capture time τ_h.

In Ref. 11 τ_h was estimated from the diffusion model as

$$\tau_h = \frac{4b^2}{\pi^2 D_h}, \qquad D_h = \frac{k_B T}{e}\mu_h, \tag{3.1}$$

where D_h is the hole diffusion coefficient, μ_h is the hole mobility in the *AlGaAs*, and $b/2$ is the width of the *AlGaAs* barrier (Fig. 2.1). The hole mobility was taken [11] from the measurements in *p*-doped *AlGaAs* bulk samples, which give $\mu_h = 4.7 \times 10^3 \mathrm{cm}^2\mathrm{V}^{-1}\mathrm{s}^{-1}$. Equation (3.1) then gives $D_h = 3.24 \mathrm{cm}^2\mathrm{s}^{-1}$ and $\tau_h = 12.5$ ps [11].

The ambipolar capture time calculated using $\tau_h = 12.5$ ps is shown by full circles in Fig. 3.1. Here we used the electron capture time (2.14)-(2.18) with a monoenergetic distribution $f_i^e(\mathbf{k}_1)$ [Eq. (2.22)], but we stress that the results in Fig. 3.1 show only a minor change when $f_i^e(\mathbf{k}_1)$ is taken as a thermalized distribution [Eq. (2.20)]. The most important result in Fig. 3.1 is a good agreement of the calculated ambipolar capture time with the measured one. Observing such agreement, the authors of Ref. 11 concluded that their diffusion model for holes [Eq. (3.1)] is reliable and the quantitative understanding of their measurements is essentially complete. We wish to show that this agreement is fortuitous and in fact obscures a much more complicated nature of the hole capture process.

First, the diffusion model (3.1) is applicable only if the hole mean free path in the *AlGaAs* barrier, ℓ, is much smaller than the barrier width, $b/2$. We estimate ℓ as

$$\ell = v_h^B \frac{m_h^B \mu_h}{e} \tag{3.2}$$

where v_h^B is the typical hole velocity on the *AlGaAs* barrier given by

$$v_h^B = \sqrt{\frac{2}{3}\frac{E_{\mathrm{excess}}}{m_e + m_h}\,\frac{m_e}{m_h}}.$$

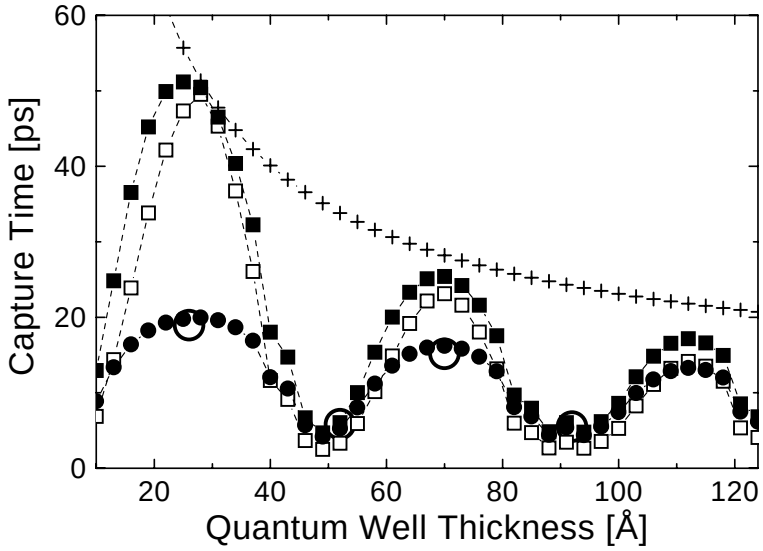

Figure 3.1: *Ambipolar capture times as a function of the QW width. The open circles show the experimental result of Ref. 11. The full circles show the ambipolar capture time calculated assuming the constant hole capture time ($\tau_h = 12.5$ ps [11]). The full squares show the same result, but with $1/\tau_h$ multiplied by the phonon emission probability in the QW (2.6). The open squares and crosses show the electron and hole capture time separately.*

We obtain $\ell = 464$ Å which is less than $b/2 = 500$ Å. This strongly suggests that the diffusion model si not applicable. In fact, the value of 464 Å even underestimates the realistic ℓ, because $\mu_h = 4.7 \times 10^3 \mathrm{cm}^2\mathrm{V}^{-1}\mathrm{s}^{-1}$ was measured [11] in *p*-doped bulk *AlGaAs* samples. In undoped *AlGaAs* barriers one can expect an order of magnitude larger μ_h, i.e., $\ell \gg b/2$. We conclude that the hole motion on the *AlGaAs* barrier is collisionless, not diffusive.

Second, even if we accept that the holes traverse the *AlGaAs* barrier within the time $\tau_h = 12.5$ ps [11], we still have to multiply τ_h^{-1} by the probability that the hole emits optical phonon when crossing the QW (otherwise the hole is not captured and leaves the QW on the other side). As demonstrated in Fig. 3.1, the ambipolar capture time with this correction (full squares) no longer agrees with experiment because the corrected hole capture time (crosses) is much longer than 12.5 ps.

Now we would like to demonstrate that the detailed semiclassical model of the hole capture developed in this work (formula 2.12, Sec. 2.1) helps to reproduce the experiment. In Fig. 3.2 the resulting ambipolar capture time (full squares) is compared with experimental data (open circles). The agreement between the theory and experiment can be considered surprisingly good, if one takes into account that the fitting constant $\tau_h = 12.5$ ps was replaced by a relatively complicated semiclassical model (2.12) without fitting parameters. In summary, the agreement supports the hole capture model, in which the photoexcited holes move across the *AlGaAs* barrier without collisions (no impurity scattering, no phonon scattering), undergo quantum reflections or transmissions on the *AlGaAs*/*GaAs* interfaces, and eventually cascade down into the *GaAs* QW by emitting optical phonons. Furthermore, this intuitively-acceptable

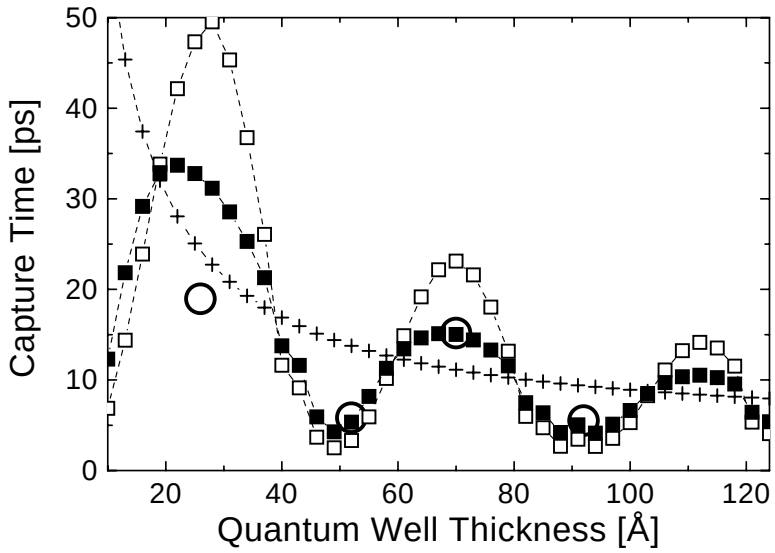

Figure 3.2: *Ambipolar capture time as a function of the QW width. The open circles show the experimental result of Ref. 11. The full squares show the ambipolar capture time calculated assuming the semiclassical capture for holes (formula 2.12). The hole capture time is shown by crosses, the electron capture time by open squares.*

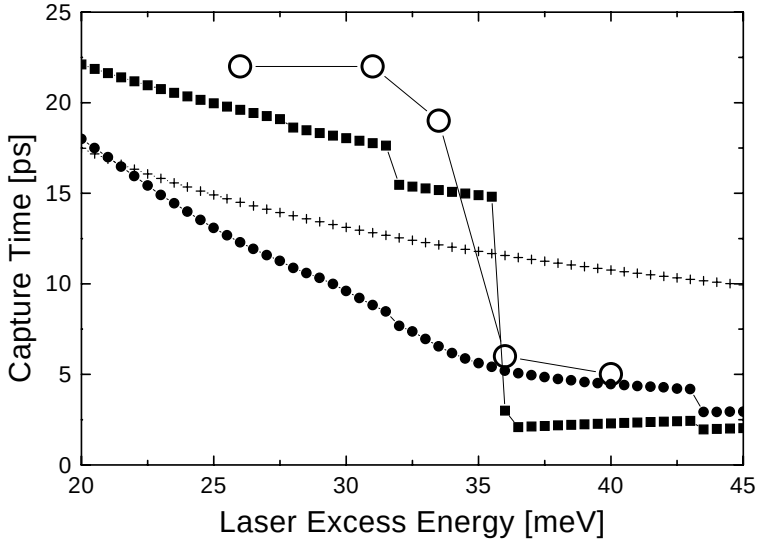

Figure 3.3: *Ambipolar capture times as a function of the laser excess energy for the* 50*-Å QW width. The experimental results of Ref. 11 (open circles) are compared with calculated ambipolar capture times. The full squares were obtained assuming a monoenergetic (δ-shaped) electron distribution above the AlGaAs barrier, the full circles assuming a thermalized (Boltzmann) electron distribution. The hole capture (crosses) was treated within the semiclassical capture model (formula 2.12).*

picture is consistent with the above mentioned arguments for the collisionless (non-diffusive) hole motion on the *AlGaAs* barriers. Only at small QW widths the theory deviates from the experiment, which likely means that at small QW widths the hole motion in the QW is no longer semiclassical.

Finally, in Fig. 3.3 the ambipolar capture time as a function of the laser excess energy is shown for the 50-Å width. The experimental results of Ref. 11 (open circles) are compared with the ambipolar capture time calculated assuming two different electron distributions above the *AlGaAs* barrier. The calculation performed with the δ-shaped electron distribution (2.22) reasonably reproduces the abrupt change of the capture time observed at the excess energy of ~ 36 meV, while the calculation performed with a thermalized electron distribution (2.20) is in a strong disagreement with experiment (it shows no abrupt change at 36 meV). These results strongly suggest that the photoexcited electron distribution above the *AlGaAs* barrier remains monoenergetic (i.e., determined by the quasi-monoenergetic laser pulse) up to the time when the capture takes place.

The abrupt change of the electron capture time can be understood as follows: The 50-Å *GaAs* QW has the second bound state very close to the top of the QW. Thus, the electrons on the *AlGaAs* barrier can be captured into the second bound state only if their excess energy is larger than the optic phonon energy (~ 36 meV). Otherwise they can only be captured into the ground QW subband, which has a much lower capture efficiency. Therefore, for the laser excess energy less than ~ 36 meV one expects a sharp increase of the capture time, which is indeed observed. Now it is easy to understand why the abrupt change of the measured capture time in Fig. 3.3 is not reproduced by the theory which assumes a thermalized electron distribution on the *AlGaAs* barrier. Such distribution has a high-energy tail with energies > 36 meV even for the excess energies much lower than 36 meV and the electrons from that tail can still be captured into the second bound state by optic phonon emission.

Chapter 4

Quantum-Mechanical Model of Electron Capture via Electron-Electron and Electron-Hole Scattering

The previous chapter was mainly focused on the optical phonon emission induced capture in the time-resolved optical measurements. We ignored the c-c scattering induced capture, because this process was negligible in the experiments of interest (we recall that the measured carrier capture time was independent on the photoexcited carrier density in a broad density range, while the c-c scattering is expected to be a density dependent process). However, in QW lasers the injected carrier densities can be much larger than the photoexcited densities in the time-resolved experiments, and the c-c scattering can be no longer negligible.

4.1 Carrier-Carrier Scattering Rate

The c-c scattering rate in the structure is treated in Born approximation according to Ref. 36. Let the carrier α occupy the subband i with wave vector $\mathbf{k}_1$ and the carrier β occupy the subband j with wave vector $\mathbf{k}_2$. Due to the mutual Coulomb interaction the carrier α is scattered into the subband m with wave vector $\mathbf{k}_1'$ and the partner carrier β is scattered into the subband n with wave vector $\mathbf{k}_2'$. The c-c scattering rate of a carrier with wave vector $\mathbf{k}_1$ from the subband i to the subband m can be obtained as

$$\lambda_{im}^{\alpha\beta}(\mathbf{k}_1) = \frac{1}{N_S A} \sum_{j,n,\mathbf{k}_2} f_j^{\beta}(\mathbf{k}_2)\, \lambda_{ijmn}^{\alpha\beta}(g), \qquad \alpha,\beta = e,h, \tag{4.1}$$

where g is a relative vector. The summation over $\mathbf{k}_2$ is assumed to include both spin orientations, the summation over j,n involves the subbands below the *AlGaAs* barrier. N_S is electron sheet density in the quantum well, A is the normalization area, $f_j^{\beta}(\mathbf{k}_2)$ is the Fermi distribution function of the carriers β in the subband j, and $\lambda_{ijmn}^{\alpha\beta}(g)$ is the c-c pair scattering rate.

The electron capture time for a model laser regime is reciprocal mean value of the electron

capture rates

$$\tau_{e-\eta}^{-1} = \frac{\sum_{i,m,\mathbf{k}_1} f_i^e(\mathbf{k}_1)\, \lambda_{im}^{e\eta}(\mathbf{k}_1)}{\sum_{i,\mathbf{k}_1} f_i^e(\mathbf{k}_1)}, \qquad \eta = e,h, \tag{4.2}$$

where the summation over i (m) includes only the electron subbands above (below) the *AlGaAs* barrier and $f_i^e(\mathbf{k}_1)$ is the proper electron distribution in the subband i. This barrier distribution function is taken for the laser regime as a constant distribution up to the polar optical phonon energy above the *AlGaAs* barrier, which roughly models the injected carriers after a rapid phonon cooling [16].

4.2 Electron-Hole Pair Scattering Rate

The e-h pair scattering rate is calculated considering the screening by electrons and holes occupying the lowest energy subband (see Appendix A). It reads

$$\lambda_{ijmn}^{eh}(g) = \frac{N_S m_r e^4}{16\pi\hbar^3\kappa^2} \int_0^{2\pi} d\theta \times \left[F_{ijmn}^{eh}(q) - \frac{q_s^e}{q\varepsilon^{eh}(q)}\, F_{i1m1}^{ee}(q) G_{1j1n}(q) + \frac{q_s^h}{q\varepsilon^{eh}(q)}\, F_{i1m1}^{eh}(q) H_{1j1n}(q) \right]^2 q^{-2}, \tag{4.3}$$

where the e-h static screening function $\varepsilon^{eh}(q)$ is given by

$$\begin{aligned}
\varepsilon^{eh}(q) &= \left(1 + \frac{q_s^e}{q} F_{1111}^{ee}(q)\right)\left(1 + \frac{q_s^h}{q} F_{1111}^{hh}(q)\right) - \frac{q_s^e}{q} F_{1111}^{eh}(q) \frac{q_s^h}{q} F_{1111}^{he}(q), \qquad (4.4)\\
G_{1j1n}(q) &= F_{1j1n}^{eh}(q)\left[1 + \frac{q_s^h}{q} F_{1111}^{hh}(q)\right] - \frac{q_s^h}{q} F_{1j1n}^{hh}(q) F_{1111}^{he}(q),\\
H_{1j1n}(q) &= F_{1j1n}^{hh}(q)\left[1 + \frac{q_s^e}{q} F_{1111}^{ee}(q)\right] - \frac{q_s^e}{q} F_{1j1n}^{eh}(q) F_{1111}^{eh}(q),\\
q &= \frac{1}{2}\left[2g^2 + \frac{4m_r}{\hbar^2} E_S^{eh} - 2g\left(g^2 + \frac{4m_r}{\hbar^2} E_S^{eh}\right)^{1/2} \cos\theta\right]^{1/2}, \qquad (4.5)
\end{aligned}$$

and $E_S^{eh} = E_i^e + E_j^h - E_m^e - E_n^h$. In the above formulae the reduced effective mass $m_r = 2m_e m_h/(m_e + m_h)$, the relative vector $\mathbf{g} = m_r(\mathbf{k}_2/m_h - \mathbf{k}_1/m_e)$, and the electron and hole subband energies are denoted as E_γ^e ($\gamma = i,m$) and E_δ^h ($\delta = j,n$), respectively. Finally, $q_s^h = e^2 m_h/(2\pi\kappa\hbar^2)\, f_1^h(\mathbf{k}_2 = 0)$.

The form factors in Eq. (4.3) are defined as

$$F_{ijmn}^{\alpha\beta}(q) = \int_{-\infty}^{\infty} dz_1 \int_{-\infty}^{\infty} dz_2\, \chi_i^\alpha(z_1)\, \chi_j^\beta(z_2)\, e^{-q|z_1 - z_2|}\, \chi_m^\alpha(z_1)\, \chi_n^\beta(z_2), \qquad \alpha,\beta = e,h, \tag{4.6}$$

where the wave function χ_γ^α of the carrier α in the subband γ ($\gamma = i,j,m,n$) is obtained assuming the x-dependent carrier effective mass and the flat Γ-band with parabolic energy dispersion, both properly interpolated between *GaAs* and *AlAs* [33].

4.3 Electron-Electron Pair Scattering Rate

The e-e pair scattering rate is found in a similar way (see Appendix A) as the e-h pair scattering rate. Taking into account only the screening by electrons in the lowest subband, one gets

$$\lambda^{ee}_{ijmn}(g) = \frac{N_S m_e e^4}{16\pi\hbar^3\kappa^2}\int_0^{2\pi} d\theta \left[F^{ee}_{ijmn}(q) - \frac{q^e_s}{q\varepsilon^e(q)}F^{ee}_{i1m1}(q)F^{ee}_{1j1n}(q)\right]^2 q^{-2}, \tag{4.7}$$

where the static screening function $\varepsilon^e(q)$ reads

$$\varepsilon^e(q) = 1+(q^e_S/q)F^{ee}_{1111}(q), \tag{4.8}$$

$$q = \frac{1}{2}\left[2g^2+\frac{4m_e}{\hbar^2}E^e_S - 2g\left(g^2+\frac{4m_e}{\hbar^2}E^e_S\right)^{1/2}\cos\theta\right]^{1/2}, \tag{4.9}$$

the relative vector $g = |\mathbf{k}_1-\mathbf{k}_2|$, and $E^e_S = E^e_i+E^e_j-E^e_m-E^e_n$. In Eq. (4.8) the static screening by the holes is omitted assuming that the holes are too slow (due to their large effective masses) to follow the fast changes of electron positions [37]. This is a so-called quasi-dynamic screening model.

It is worth mentioning that the screening [i.e. the term containing the screening function $\varepsilon^e(q)$] disappears in Eq. (4.7) for those transitions in which $F^{ee}_{i1m1}(q)=0$ and/or $F^{ee}_{1j1n}(q)=0$. This happens when $\chi^e_i(z_1)$ is symmetric (antisymmetric) and $\chi^e_m(z_1)$ is antisymmetric (symmetric), and/or when the same holds for $\chi^e_j(z_2)$ and $\chi^e_n(z_2)$.

For example, when the QW contains two energy subbands, the screening effect disappears for the transitions $i,1\to 1,2$ $(i=3,5,\dots)$. Then the e-e pair scattering rate reads

$$\lambda^{ee}_{i112}(g) = \frac{N_S m_e e^4}{16\pi\hbar^3\kappa^2}\int_0^{2\pi} d\theta \,\frac{\left[F^{ee}_{i112}(q)\right]^2}{q^2}. \tag{4.10}$$

Note that the same effect appears also in the e-h pair scattering rate (4.3).

After simple manipulations, the integrand in Eq. (4.7) can be simplified assuming

$$\frac{F^{ee}_{ijmn}(q)F^{ee}_{1111}(q)}{F^{ee}_{i1m1}(q)F^{ee}_{1j1n}(q)} \approx 1 \tag{4.11}$$

into the form [36]

$$\lambda^{ee}_{ijmn}(g) = \frac{N_S m_e e^4}{16\pi\hbar^3\kappa^2}\int_0^{2\pi} d\theta \,\frac{|F^{ee}_{ijmn}(q)|^2}{q^2\,\varepsilon^e(q)^2}. \tag{4.12}$$

To justify the approximation (4.11), the e-e capture times calculated for various screening functions are compared in Fig. 4.1. In this calculation the electron distribution function $f^e_i(\mathbf{k}_1)$ in the formula (4.2) was taken as a constant distribution up to the polar optical phonon energy above the *AlGaAs* barrier. The capture time obtained from the pair scattering rate (4.12) with the screening function (4.8) is almost the same as the capture time obtained from the pair scattering rate (4.7). If (following Ref. 38) we use Eq. (4.12) with $F^{ee}_{1111}(q)=1$ in the screening function (4.8), the calculated capture time overestimates both capture times more than by 20%.

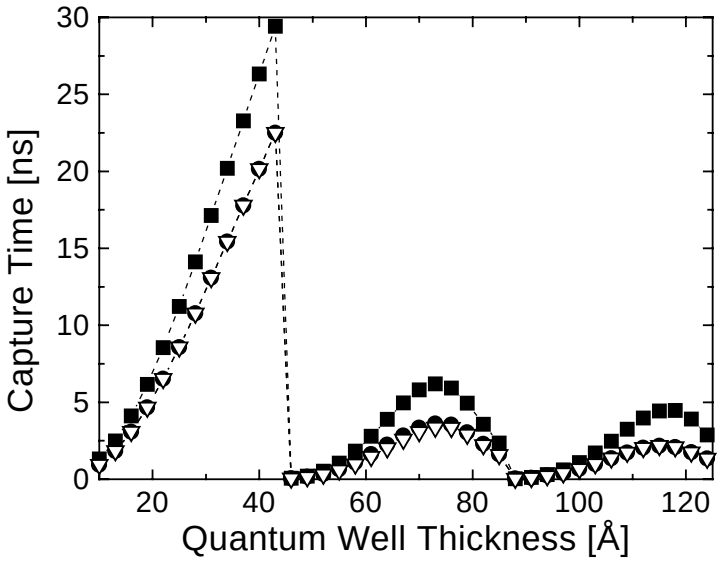

Figure 4.1: *e-e capture time as a function of the QW width for various static screening models. The capture time calculated using the e-e scattering rate (4.7) [open triangles] is compared with the capture times calculated using the e-e scattering rate (4.12) screened by the screening function (4.8) with realistic $F_{1111}(q)$ [full circles] and with $F_{1111}(q) = 1$ [full squares].*

4.4 Electron-Electron Pair Scattering Rate with Degeneracy and Exchange

To include the Pauli exclusion principle in the e-e scattering rate (4.7) we can start from the equation

$$\lambda^{ee}_{ijmn}(g) = \frac{N_S m_e e^4}{8\pi\hbar^3\kappa^2} \int d\mathbf{k}_2' \left[1 - f^e_m(\mathbf{k}_1 + \mathbf{k}_2 - \mathbf{k}_2')\right] \left[1 - f^e_n(\mathbf{k}_2')\right] \times \frac{\left[F^{ee}_{ijmn}(q_l)\right]^2}{q_l^2 \varepsilon^e(q_l)^2} \delta\left[\frac{\hbar^2}{2m_e}(\mathbf{k}_1{}^2 + \mathbf{k}_2{}^2 - \mathbf{k}_1'{}^2 - \mathbf{k}_2'{}^2) + E^e_S\right], \quad (4.13)$$

in which $\mathbf{k}_1' = \mathbf{k}_1 + \mathbf{k}_2 - \mathbf{k}_2'$. Equation (4.13) may be transformed to polar axes as

$$\lambda^{ee}_{ijmn}(g) = \frac{N_S m_e e^4}{8\pi\hbar^3\kappa^2}\int_0^{2\pi} d\theta \int_0^{\infty} dk_2' \quad k_2'\{1 - f^e_m \times$$
$$\times \left(\frac{\hbar^2}{2m_e}[k_1^2 + k_2^2 + {k_2'}^2 - 2k_1k_2\cos\phi - 2k_1k_2'\cos\theta + 2k_2k_2'\cos(\theta-\phi)] + E^e_m - E_F\right)\}$$
$$\times \left\{1 - f^e_n(\frac{\hbar^2}{2m_e}{k_2'}^2 + E^e_n - E_F)\right\}\frac{\left[F^{ee}_{ijmn}(q_l)\right]^2}{q_l^2\varepsilon^e(q_l)^2}$$
$$\times \delta\left(\frac{\hbar^2}{m_e}[k_1k_2'\cos\theta - {k_2'}^2 - k_1k_2\cos\phi + k_1k_2'\cos(\theta-\phi)] + \frac{1}{2}E^e_S\right), \quad (4.14)$$

The delta function simplifies the integration over k_2' in Eq. (4.14) and the e-e pair scattering rate with degeneracy is then given by

$$\lambda^{ee}_{ijmn}(g) = \frac{N_S m_e e^4}{8\pi\hbar^3\kappa^2}\sum_{l=1}^{2}\int_0^{2\pi} d\theta \,\frac{p_l}{|D-2p_l|}\,[1 - f^e_m(r_l)]\,[1 - f^e_n(p_l)]\,\frac{\left(F^{ee}_{ijmn}(q_l)\right)^2}{q_l^2\varepsilon^e(q_l)^2}, \quad (4.15)$$

where

$$\begin{aligned}
q_l &= [{p_l}^2 + k_2^2 - 2k_2p_l\cos(\theta-\phi)]^{1/2}, \qquad l = 1,2\\
r_l &= [k_1^2 + k_2^2 + p_l - 2k_1k_2\cos\phi - 2k_1p_l\cos\theta + 2k_2p_l\cos(\theta-\phi)]^{1/2},\\
p_1 &= \frac{1}{2}D + \frac{1}{2}\left[D^2 + \frac{4m}{\hbar^2}E^e_S - 4k_1k_2\cos\phi\right]^{1/2},\\
p_2 &= \frac{1}{2}D - \frac{1}{2}\left[D^2 + \frac{4m}{\hbar^2}E^e_S - 4k_1k_2\cos\phi\right]^{1/2},\\
D &= k_1\cos\theta + k_2\cos(\theta-\phi).
\end{aligned}$$

The angles θ and ϕ in the above expressions are between the wave vectors $\mathbf{k}_1, \mathbf{k}_2'$ and $\mathbf{k}_1, \mathbf{k}_2$; respectively.

Electrons are indistinguishable particles. Therefore, the scattering rate (4.7) should include the exchange effect [37]. According to Ref. 36 the exchange can be incorporated into the intersubband e-e scattering rate (4.15) using the replacement

$$\frac{|F^{ee}_{ijmn}(q_l)|^2}{q_l^2\varepsilon^e(q_l)^2} \mapsto \frac{1}{2}\left[\frac{|F^{ee}_{ijmn}(q_l)|^2}{q_l^2\varepsilon^e(q_l)^2} + \frac{|F^{ee}_{ijnm}(q_l')|^2}{{q_l'}^2\varepsilon^e(q_l')^2} - \frac{F^{ee}_{ijmn}(q_l)F^{ee}_{ijnm}(q_l')}{q_l\varepsilon^e(q_l)q_l'\varepsilon^e(q_l')}\right], \quad (4.16)$$

where

$$q_l' = [{p_l}^2 + k_1^2 - 2k_1p_l\cos(\theta)]^{1/2}, \qquad l = 1,2.$$

Chapter 5

Electron Capture Time in Conditions of the Lasing Quantum Well

5.1 Electron-Electron and Electron-Hole Capture Times

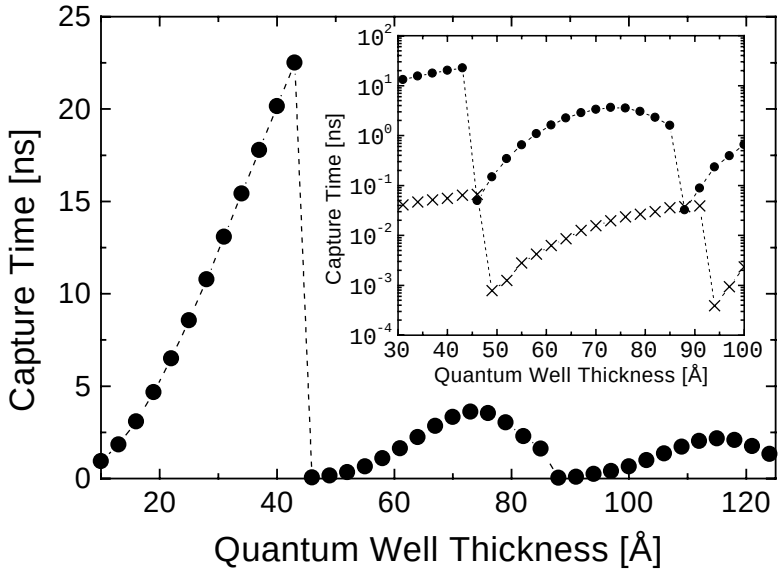

Figure 5.1: *e-e capture time τ_{e-e} vs. the QW thickness for $N_S = 10^{11}\mathrm{cm}^{-2}$. In the inset these results are compared with the data (crosses) from Ref. 18.*

Full circles in Fig. 5.1 show the e-e interaction induced capture time, τ_{e-e}, versus the QW width. The distribution $f_i(\mathbf{k}_1)$ in the formula (4.2) was taken as a constant distribution up to 36.8 meV above the *AlGaAs* barrier, which roughly models the injected "barrier" distribution after a rapid phonon cooling in the lasing QW [16, 18]. Another characteristic feature of the lasing QW structure is a high carrier density in the QW ($N_S = 10^{11}\mathrm{cm}^{-2}$ considered in Fig. 5.1

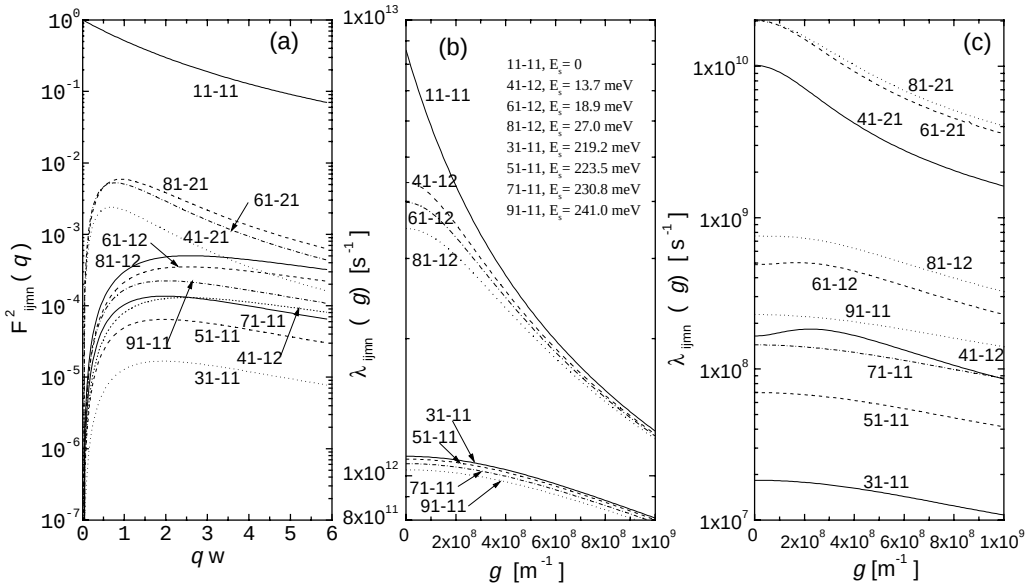

Figure 5.2: *(a) Square of the e-e scattering form factor $F_{ijmn}(q)$ as a function of wave vector q for a QW with thickness $w = 49$ Å. The indices i, j and m, n label the initial and final subband states, respectively. States $1, 2$ are bound in the QW, states $3, 4, \cdots, 9$ have subband energies above the AlGaAs barrier. Except for the transition $11 - 11$ all other transitions are the e-e capture transitions. (b,c) e-e scattering rate λ_{ijmn} vs the relative wave vector size g. (b) Calculation with $F_{ijmn} = 1$. (c) Calculation with form factors from Fig. 5.2a.*

is the lower limit).

In the inset our calculation is compared with the results (crosses) of Ref. 18. Both τ_{e-e} curves oscillate with the QW width and reach the resonant minimum, whenever a new bound state merges into the QW. The shift of our resonance minima to slightly lower QW widths is due to different effective masses in *GaAs*, *AlGaAs* and *AlAs*, which we considered when we calculated the electron wave functions [21]. However, our τ_{e-e} is two-to-three orders of magnitude larger. The difference of a factor of 4 is due to the missing factor of $1/4$ in the e-e scattering rate of Ref. 18 (see Ref. 36 for details). When the τ_{e-e} values from Ref. 18 are multiplied by a factor of 4, our τ_{e-e} is still ~ 100 times larger. We would like to give arguments in the following that our results are correct.

The electron capture rate in the QW actually represents the transition of an electron from the quasi-2D state over a barrier into a quasi-2D bound state in the well. The transition rate is governed by the respective form factor [see formulae (4.1), (4.12) and (4.6)] which is determining the order of the electron capture rate. The maximum contributions of the form factors to the electron capture rate can be identified in Fig. 5.2a where $qw \approx 1$. The same holds for the e-e interaction induced capture time and for the e-pop interaction induced capture time [20].

In order to provide insight let us consider the QW with width $w = 49$ Å. To demonstrate

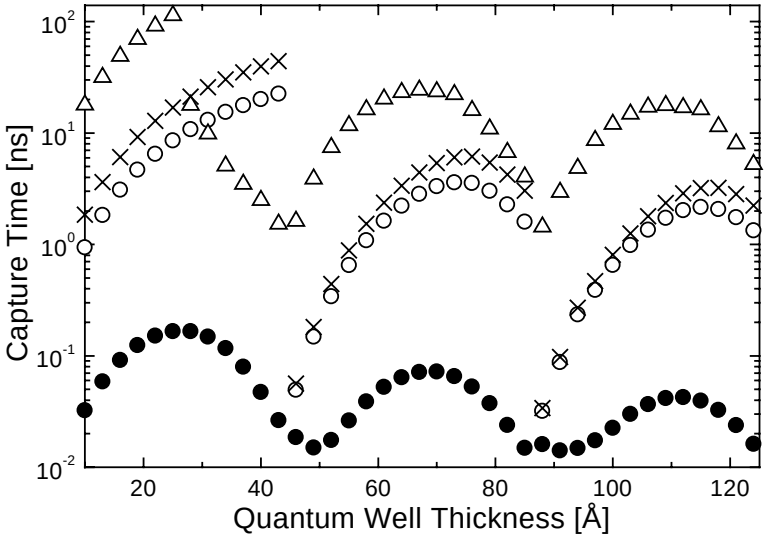

Figure 5.3: *Electron capture time vs the QW width for the e-pop interaction (full circles), the e-h interaction (open triangles), the e-e interaction without exchange effect (open circles), and the e-e interaction with exchange effect (crosses).*

how the form factor affects the e-e scattering rate, we compare in Fig. 5.2c $\lambda_{ijmn}(g)$ as obtained using $F^2_{ijmn}(q)$, shown in Fig. 5.2a, with $\lambda_{ijmn}(g)$ obtained with $F^2_{ijmn} = 1$. The latter is typically between $\sim 10^{12}\mathrm{s}^{-1}$ and $\sim 4\times 10^{12}\mathrm{s}^{-1}$ for all capture transitions and its dependence on i, j, m, n is simply manifested through E_S. Figure 5.2c shows a quite different behavior and the relative importance of the individual capture transitions is determined by the behavior of the form factors (Fig. 5.2a). The individual capture times are at least two orders of magnitude larger than the subpicosecond capture times shown in Fig. 5.2c. The subpicosecond e-e scattering is characteristic for intrasubband transitions as illustrated in Fig. 5.2b for $\lambda_{1111}(g)$ [$\lambda_{1111}(g)$ in Fig. 5.2b is rather inaccurate because $F_{1111} = 1$, but it still agrees reasonably with similar calculations of Refs. 39 and 40]. We cannot explain why Ref. 18 predicts much smaller e-e capture times within essentially the same model (we could only reproduce the published form factors [18]).

Figure 5.3 shows the electron capture time versus the QW width for the e-e, e-h, and e-pop interactions where, in case of the e-e interaction, the results obtained with and without exchange effect are distinguished. In these calculations the function $f^e_i(\mathbf{k}_1)$ in the formula (4.2) is also taken as a constant distribution up to the polar optical phonon energy above the *AlGaAs* barrier. At small QW widths, when the QW contains only one bound state, the e-h and e-e capture times increase with an increasing QW width. At QW widths at which the second bound state merges into the QW (~ 30 Å for holes, 46 Å for electrons), the e-h and e-e capture times decrease suddenly by several orders of magnitude. With a further increase of the QW width the oscillatory behavior persists, but the oscillations become smooth.

To understand this feature in Fig. 5.4a we split the total e-e capture time from Fig. 5.3 into the e-e capture time to states $1,1$ (full squares) and the e-e capture time to states $1,2$ and $2,1$ (full triangles). A smooth decrease of the total capture time from its maximum value at $w = 73$ Å

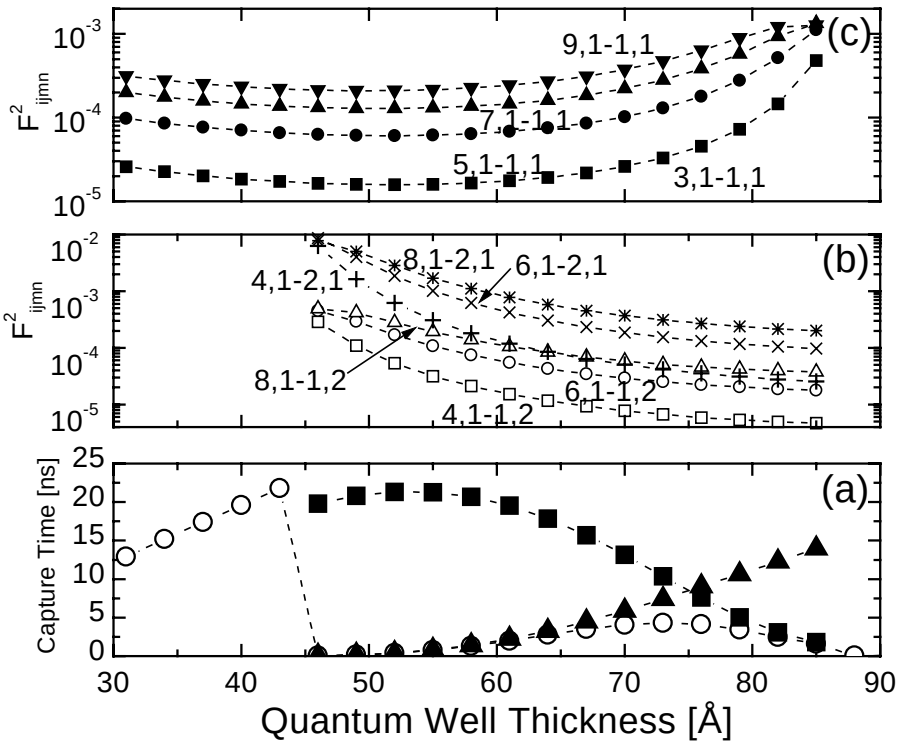

Figure 5.4: *(a) e-e capture time vs the QW width. The total e-e capture time from Fig. 5.3 (open circles) is split into the e-e capture time to state* $1,1$ *(full squares) and into the e-e capture time to states* $1,2$ *and* $2,1$ *(full triangles). (b) Squares of the e-e form factors* F_{i112} *and* F_{i121} *vs the QW width for* $q = 3\times10^8\mathrm{m}^{-1}$*. (c) Squares of the e-e form factors* F_{i111} *vs the QW width for* $q = 3\times10^8\mathrm{m}^{-1}$*.*

is due to the decrease of the capture time to states $1,1$ with *w*. This decrease is caused by the increase of relevant form factors (Fig. 5.4c) with *w*. At the same time the capture time to state $1,2$ and $2,1$ increases with *w* due to the decrease of relevant form factors (Fig. 5.4b) with *w*. Similar conclusions can be also done for the e-h capture.

5.2 Electron-Polar Optical Phonon Capture Time

Figure 5.5 compares the e-pop interaction induced capture time, τ_{e-pop}, with τ_{e-e} where again the constant distribution $f_i(\mathbf{k}_1)$ was taken. The τ_{e-pop} data shown by empty circles are calculated using the same static screening $\varepsilon(q)$ as for the e-e scattering, empty squares show τ_{e-pop} for $\varepsilon(q) = 1$. A more accurate calculation with dynamic screening will give results between these two extreme cases. We can conclude that τ_{e-e} is one-to-three orders larger than τ_{e-pop} except for QW widths near the resonance minima. This conclusion differs from the previous analysis [18] which predicts nearly the same oscillation amplitude in both cases. Ref. 18 also predicts that in the SCHQW lasers with a QW width below 40 Å the e-e capture causes signifi-

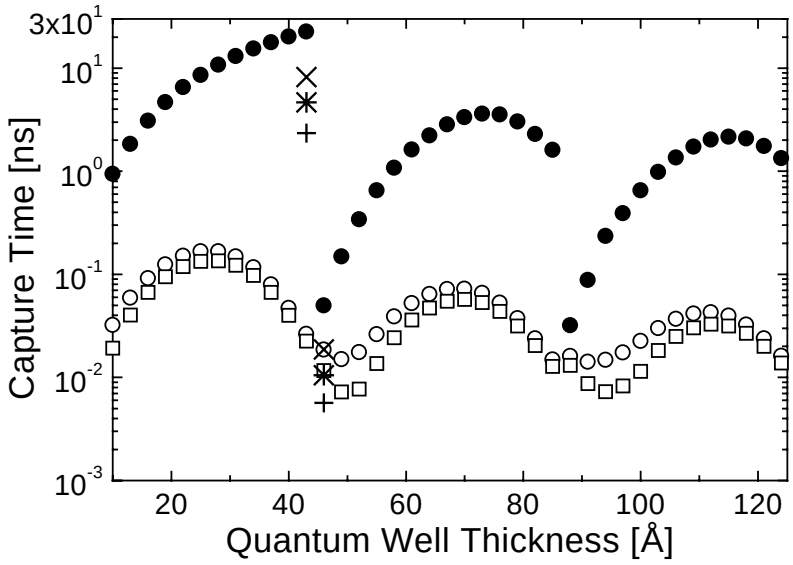

Figure 5.5: *e-pop capture time τ_{e-pop} and e-e capture time τ_{e-e} vs the QW thickness for $N_S = 10^{11}\text{cm}^{-2}$. Open circles show τ_{e-pop} for the statically screened e-pop interaction, open squares show τ_{e-pop} for the unscreened e-pop interaction and full circles are the τ_{e-e} data from Fig. 5.1. Crosses, asterisks and pluses at* 43 *Å and* 46 *Å show the τ_{e-e} data for $N_S = 2.8\times10^{11}\text{cm}^{-2}, 5\times10^{11}\text{cm}^{-2}$ and 10^{12}cm^{-2}, respectively.*

cant excess carrier heating in the QW. Figure 5.5 does not support this conclusion, because the e-e capture is negligible.

The τ_{e-pop} curve in Fig. 5.5 does not show any resonant drop for QW widths of 46 Å and 88 Å, because the barrier electrons occupy the states below the threshold for polar optical phonon emission and cannot be scattered into the subband which is in resonance with the top of the QW. A further increase of the QW width shifts the resonant subband deeper into the QW and the e-pop scattering into this subband smoothly increases. The exception is a monoenergetic distribution with energy close to the polar optical phonon energy. In such case the e-pop scattering into the resonance subband is not prohibited and a resonant decrease of the e-pop capture time takes place [41].

To show the role of form factors, Figs. 5.6b and 5.6c compare the unscreened e-pop scattering rates obtained using F_{iimm} from Fig. 5.6a with the rates obtained with $F_{iimm} = 1$. The individual e-pop capture rates in Fig. 5.6c are governed by relevant form factors, while for $F_{iimm} = 1$ (Fig. 5.6b) one only finds a simple dependence on P. Compared to the e-e scattering rates in Fig. 5.2c, the corresponding rates in Fig. 5.6c are systematically higher because the e-pop capture rate (2.14) depends on F_{iimm} linearly while the e-e scattering rate (4.12) depends on F_{ijmn} quadratically. This fact naturally makes the e-e capture less effective than the e-pop capture except for high electron densities.

Similarly to the e-e interaction case, in Fig. 5.7a we split the total e-pop capture time from Fig. 5.5 into the e-pop capture time to states $1,1$ (open squares) and the e-pop capture time to

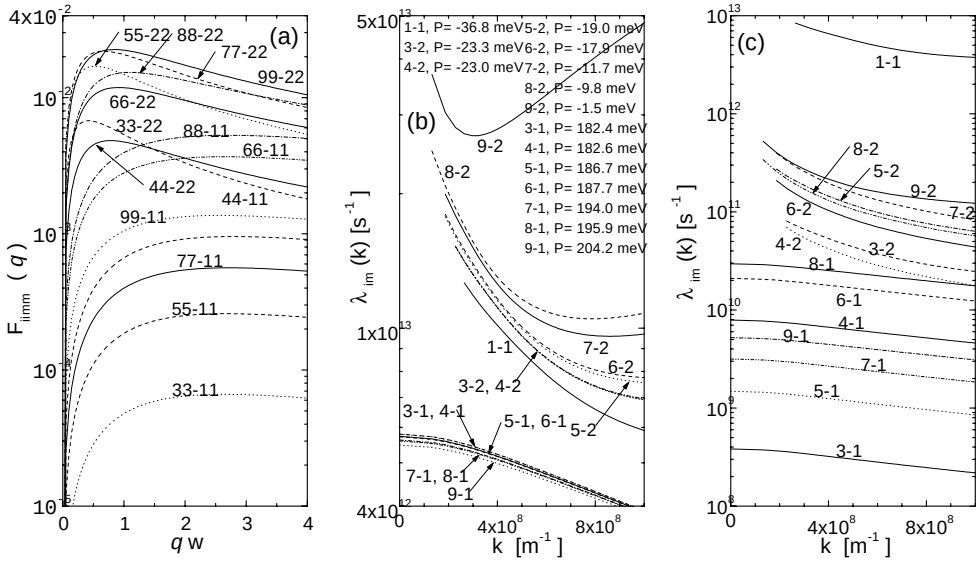

Figure 5.6: *(a) The e-pop scattering form factors $F_{iimm}(q)$ [see the text] are shown for comparison. (b,c) e-pop scattering rate λ_{im} vs the wave vector k for the QW with width $w = 49$ Å. (b) Calculation with $F_{iimm} = 1$. (c) Calculation with form factors from Fig. 5.6a.*

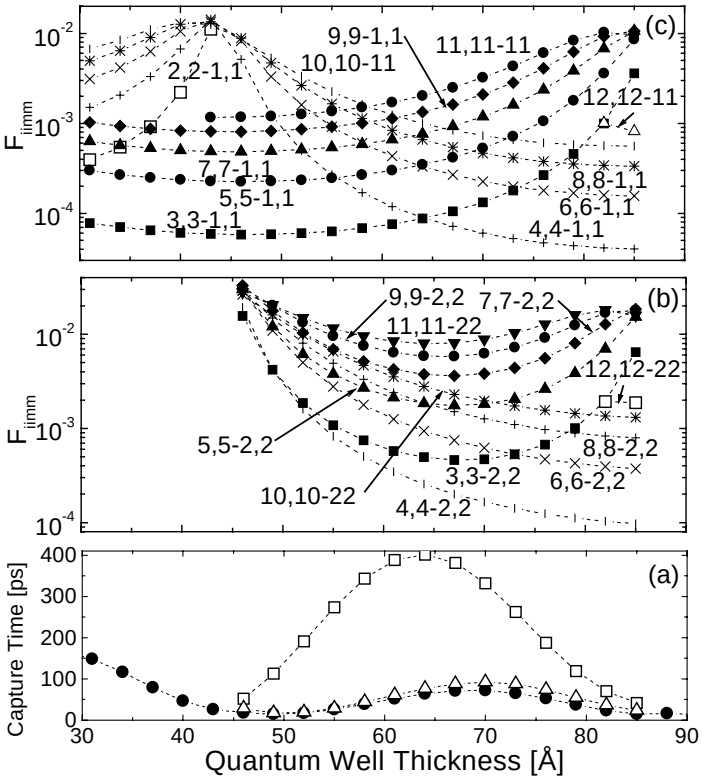

Figure 5.7: *(a) e-pop capture time vs the QW width. The total e-pop capture time (full circles) from Fig. 5.5 is split into the e-pop capture time to state $1,1$ (open squares) and into the e-pop capture time to state $2,2$ (open triangles). (b) The e-pop form factors F_{ii22} vs the QW width for $q = 3 \times 10^8 \mathrm{m}^{-1}$. (c) The e-pop form factors F_{ii11} vs the QW width for $q = 3 \times 10^8 \mathrm{m}^{-1}$.*

states 2,2 (open triangles). The transitions to the highest subband in the QW always play a more important role than transitions to lower subbands. This fact is explained by the behavior of relevant form factors in Figs. 5.7b and 5.7c.

It is easy to assess the dependence of the capture times on the electron density N_S. For $N_S \geq 10^{11}\text{cm}^{-2}$ and temperature 8 K the static screening $\varepsilon(q)$ is independent on N_S, because $f_1(0) \simeq 1$. Therefore, the τ_{e-pop} values in Fig. 5.5 would be the same also for higher N_S and the τ_{e-e} values would decrease approximately like N_S^{-1} for each QW width. In Fig. 5.5 we show τ_{e-e} for $N_S = 2.8\times10^{11}\text{cm}^{-2}, 5\times10^{11}\text{cm}^{-2}$ and 10^{12}cm^{-2} only at QW widths of 43 Å and 46 Å. At 43 Å, τ_{e-e} is much larger than τ_{e-pop} even for $N_S = 10^{12}\text{cm}^{-2}$ due to the absence of resonance. At 46 Å, when the first excited subband merges into the QW, τ_{e-e} resonantly decreases by about 500 times and becomes smaller than τ_{e-pop} when $N_S \simeq 5\times10^{11}\text{cm}^{-2}$. When $N_S = 10^{12}\text{cm}^{-2}$, the total capture time $\tau_{e-e}\tau_{e-pop}/(\tau_{e-e}+\tau_{e-pop})$ is 3.8 ps for unscreened e-pop capture ($\tau_{e-pop} = 11$ ps) and 4.3 ps for screened e-pop capture ($\tau_{e-pop} = 18$ ps). Thus, compared to the case $\tau_{e-e}^{-1} = 0$ the capture efficiency of the QW with the optimized (resonant) width can be improved with a factor $2.9-4.2$ by increasing N_S to 10^{12}cm^{-2}. At higher densities, which are investigated later, the capture time is expected to increase with N_S on the basis of the results of Refs. 41 and 42. For $N_S > 10^{12}\text{cm}^{-2}$ it is no longer justified to treat the e-e and e-pop scattering separately [41, 42], because the electrons interact with a coupled system of electrons and phonons.

5.3 Dependence of Electron Capture Time on Quantum Well Depth

To directly detect the e-e capture time it is necessary to suppress the e-pop interaction [21]. A proper structure for the e-pop interaction suppression is the structure with the QW depth smaller than the polar optical phonon energy. If in the time-resolved optical experiment [11] such structure was irradiated by a short laser pulse, the excited carriers above the barrier would thermalize to the Boltzmann distribution with the electron temperature T_e within several picoseconds [11, 43] and after that they would be captured via the e-e interaction into the QW. Figure 5.8 shows the electron capture time versus the QW depth for the QW width equal to 46 Å. Here we assume that the QW depth varies with the aluminium content x according to the relation $V_w = (0.9456x + 0.1288x^2)$ eV [33]. In this calculation the distribution function $f_i^e(\mathbf{k}_1)$ in the capture time formula (4.2) is taken as the Boltzmann distribution function at the electron temperature $T_e = 70$ K. This choice corresponds to the assumption that the electrons are optically excited only a few meV above the *AlGaAs* barrier. Figure 5.8 also shows that the e-e capture dominates if the QW depth is less than 0.04 eV. Degeneracy and exchange affect the e-e capture time substantially at small QW depth. At the QW depth at which the second bound state of the hole merges into the QW (~ 0.11 eV), the e-h capture time is smaller than the e-e capture time (except near the resonance) but still greater than the e-pop capture time. Therefore, the effect of the e-h capture time can be neglected even in the resonance minimum.

The electron capture times from Fig. 5.9 illustrate the inclusion and exclusion of the degeneracy and exchange effect in the e-e interaction with the increasing electron density for a shallow

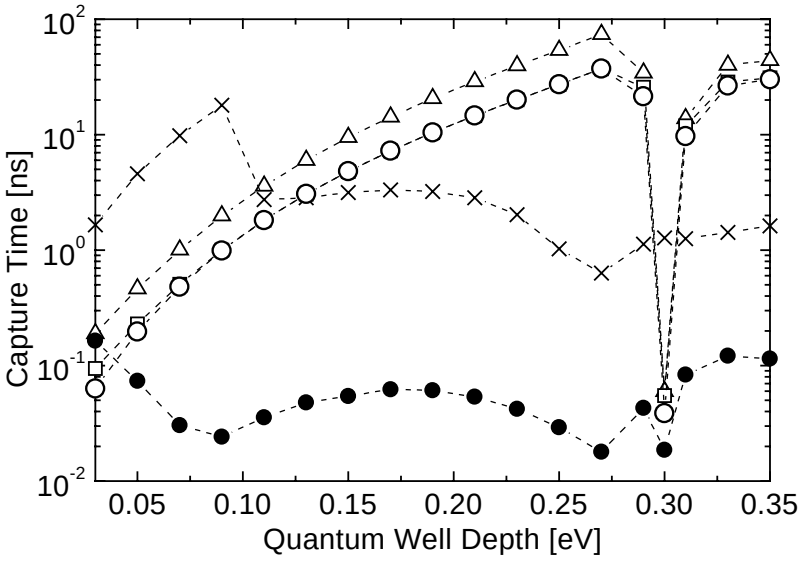

Figure 5.8: *Electron capture time as a function of the QW depth for the QW width of* 46 *Å. Open circles are for the e-e interaction without degeneracy and exchange effect, open squares are for the e-e interaction with degeneracy, open triangles are for the e-e interaction with degeneracy and exchange effect, crosses are for the e-h interaction, and full circles are for the e-pop interaction induced capture time. In the calculations the distribution function* $f_i^e(\mathbf{k}_1)$ *in the capture time formula (4.2) is the Boltzmann distribution at the electron temperature* 70 *K.*

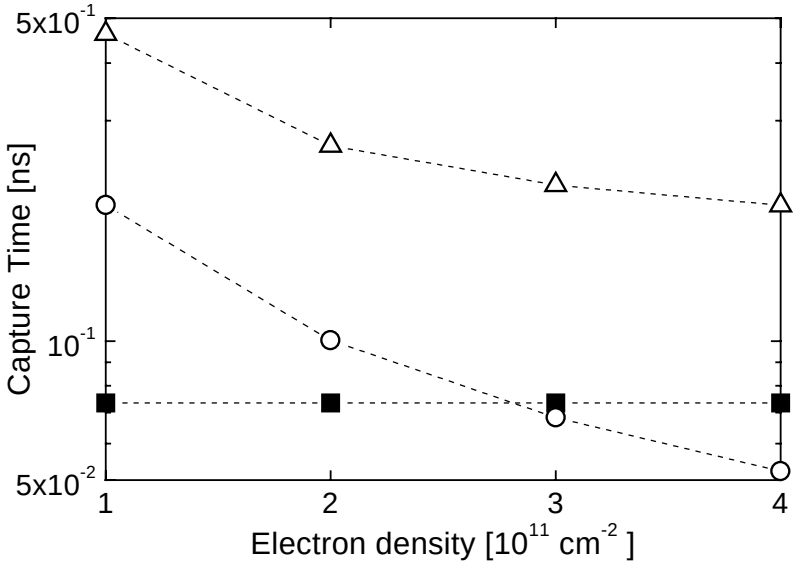

Figure 5.9: *Electron capture time vs the electron density for the QW with* $V_w = 0.05$ *eV and* $w = 46$ *Å. Open circles (triangles) represent the capture time for the e-e interaction without (with) degeneracy and exchange effect, respectively, and full squares represent the capture time for the e-pop interaction.*

QW ($V_w = 0.05$ eV, $w = 46$ Å). In such structures, recently also considered in Ref. 44, the e-e capture time is of similar importance as the e-pop capture time for higher electron densities although it was calculated including the degeneracy and exchange effect in the e-e interaction which increases the capture time by about two times.

Outside the resonance, the exchange increases the e-e capture time by about two times due to the following reasons: In case that both electrons are scattered into the same subband ($m = n$), all three terms in the substitution (4.16) have almost the same magnitude (which we verify numerically) because the values of q and q' are very close. In case that both electrons are scattered into different subbands ($m \neq n$), it is necessary to take into account that the substitution (4.16) is summed in the formulae (4.1) and (4.2) over the final states m and n. The sum the terms with final states m, n and n, m can be rewritten as

$$\frac{1}{2}\left[\frac{|F_{ijmn}(q)|^2}{q^2\varepsilon(q)^2}+\frac{|F_{ijnm}(q)|^2}{q^2\varepsilon(q)^2}\right]+\frac{1}{2}\left[\frac{|F_{ijnm}(q')|^2}{q'^2\varepsilon(q')^2}+\frac{|F_{ijmn}(q')|^2}{q'^2\varepsilon(q')^2}\right] - \frac{1}{2}\left[\frac{F_{ijmn}(q)F_{ijnm}(q')}{q\varepsilon(q)q'\varepsilon(q')}+\frac{F_{ijnm}(q)F_{ijmn}(q')}{q\varepsilon(q)q'\varepsilon(q')}\right]. \quad (5.1)$$

All three terms in Eq. (5.1) have almost the same magnitude which we verify numerically. Consequently, the presence of the third (interference) term decreases the value of the expression (5.1) two times in comparison with the case when the exchange effect (i. e., the interference term) is neglected. Finally, in the resonance the exchange increases the capture time only by 10%. This is due to the fact that in the resonance the values of q and q' strongly differ and the interference term becomes much smaller than direct terms.

The effect of degeneracy on the capture time is negligible when the difference between the lowest energy subband above the barrier and the highest energy subband in the QW is large compared to the quasi-Fermi energy of the electrons in the QW. In such case most of final states in the QW are unoccupied and the e-e capture times with and without degeneracy are quite close. Near the resonance, when the highest energy subband in the QW is close to the lowest subband above the barrier, the degeneracy strongly reduces the number of available final states despite the fact that the highest subband is essentially unoccupied. This is due to the fact that an electron captured in the highest subband of the QW can exchange only a small amount of energy with a scattering partner in the lowest subband of the QW. The available final states of the scattering partner are therefore blocked by the 8-K Fermi distribution in the QW.

5.4 Total Carrier Capture Time

The total electron capture time τ_e, which includes the e-e, e-h and e-pop capture times, can be obtained as

$$\frac{1}{\tau_e} = \frac{1}{\tau_{e-e}} + \frac{1}{\tau_{e-h}} + \frac{1}{\tau_{e-pop}} \quad . \quad (5.2)$$

In Fig. 5.10 the e-pop capture time (open squares) is compared with the total electron capture time (full circles) obtained using the e-e capture time with exchange and the e-h capture time

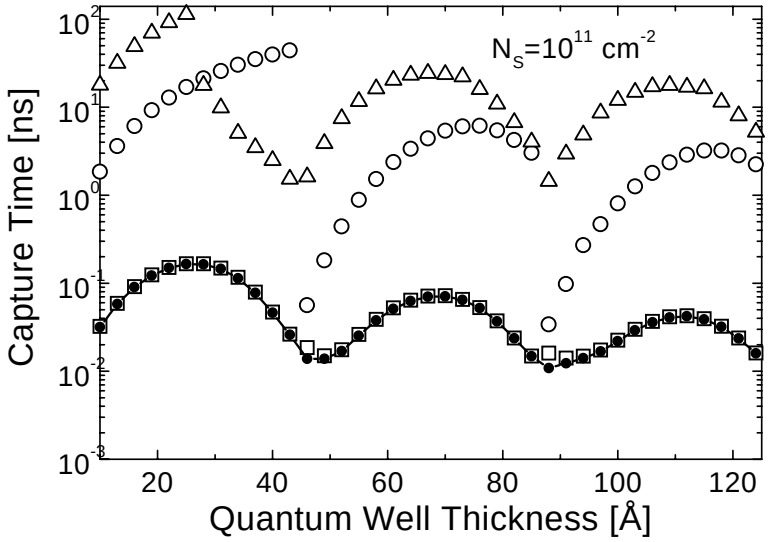

Figure 5.10: *Total electron capture time vs the QW width for the electron density* $10^{11}\mathrm{cm}^{-2}$ *(full circles) is compared with the e-pop capture time (open squares). Electron capture times via the e-e interaction with the exchange effect (open circles) and via the e-h interaction (open up triangles) are also shown for the same electron density.*

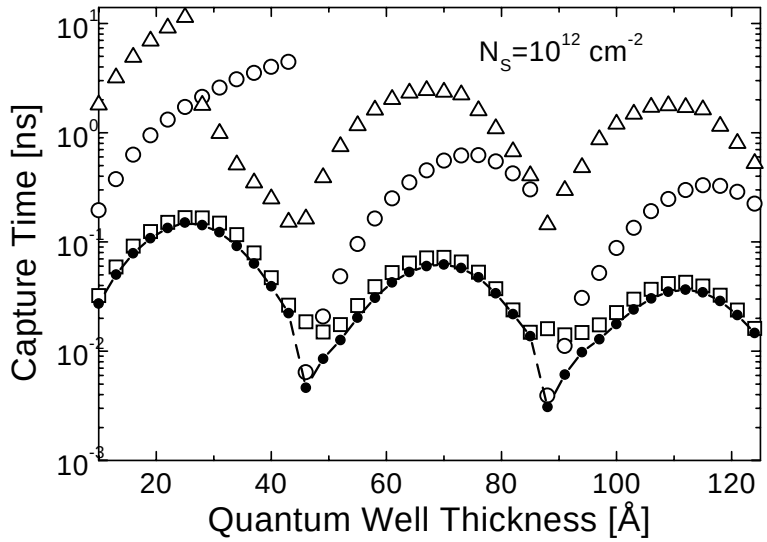

Figure 5.11: *The same material as in the Fig. 5.10 but for the electron density* $10^{12}\mathrm{cm}^{-2}$*.*

for the carrier density $N_S = 10^{11}\mathrm{cm}^{-2}$ in the formula (5.2). The same material but for $N_S = 10^{12}\mathrm{cm}^{-2}$ is in Fig. 5.11.

	Symbol	*Value*	*Ref*
Static permittivity	κ	13.0	[45]
High-frequency permittivity	κ_∞	10.9	[46]
Mass density (*GaAs*)	ρ	5317.6 $\mathrm{kg\,m^{-3}}$	[46]
Energy of the polar optical phonon	$\hbar\omega_{LO}$	36.8 meV	[47]
Energy of the nonpolar optic phonon	$\hbar\omega_0$	35.34 meV	[45]
Related to electron			
Potential between the QW and barrier	V_w	0.3 eV	[11]
Potential between the barrier and cladding layer	V_b	1.07 eV	[33]
Effective mass in the QW (*GaAs*)	m_e	0.0665	[33]
Effective mass in the barrier ($Al_{0.3}Ga_{0.7}As$)	m_e^B	0.0984	[33]
Effective mass in the cladding layer (*AlAs*)	m_e^C	0.1808	[33]
Related to heavy hole			
Potential between the QW and barrier	V_w^h	0.135 eV	[33]
Potential between the barrier and cladding layer	V_b^h	0.5057 eV	[33]
Effective mass in the QW (*GaAs*)	m_h	0.44	[34]
Effective mass in the barrier ($Al_{0.3}Ga_{0.7}As$)	m_h^B	0.489	[45]
Effective mass in the cladding layer (*AlAs*)	m_h^C	0.72	[45]
Non-polar optic phonon deformation potential	D_0	8.9×10^{10} eV/Å	[47]

Table 5.1: Material parameters for SCHQW used in the calculations

Chapter 6

Summary

1. Following the goals 1, 2 and 3 (Sec. 1.3) we have calculated (Chaps. 2 and 3) the ambipolar carrier capture time in a SCHQW excited by a short laser pulse. This ambipolar capture time incorporates the semiclassical hole capture time and the quantum-mechanical electron capture time. The latter one, calculated for the e-pop interaction, oscillates as a function of the QW width. The calculated ambipolar capture time reasonably agrees with the measured capture time, which suggests that our semiclassical thermionic model of the hole capture is reasonable. Furthermore, our analysis of the electron distribution function in the SCHQW barrier shows that the photoexcited electrons are nonthermal before they are captured in the QW.

2. Following the goals 4 and 6 (Sec. 1.3) we have calculated (Chaps. 4 and 5) the electron capture times due to the e-e, e-h and e-pop interactions for a model laser regime. The calculated capture times oscillate as a function of the QW width with the same period, but with quite different amplitudes. For the electron density of $10^{11}\mathrm{cm}^{-2}$ in the QW, the e-e capture time is one to three orders larger and the e-h capture time two to four orders larger than the e-pop capture time. The exceptions are the QW widths near resonance minima, where the e-e capture time is only $2-3$ times larger. With increasing density the e-e capture time decreases and for a high enough density ($10^{12}\mathrm{cm}^{-2}$) becomes smaller than the e-pop capture time. Therefore, in simulations of the QW lasers the e-e interaction should be taken into account at resonance for any density $> 10^{11}\mathrm{cm}^{-2}$.

3. In accord with the goal 5, we have taken into account (Chap. 4) the effects of exchange and degeneracy on the e-e capture. The exchange effect increases the e-e capture time approximately two times while the degeneracy does not change the capture time except for the QW depths and widths near the resonance.

4. We have shown (Secs. 5.1 and 5.2) that the oscillatory behaviour of the e-e and e-pop capture time has a different physical origin.

5. About the goal 7 (Sec. 1.3). The oscillation minima of the calculated capture times occur at the QW widths of ~ 50 Å and ~ 90 Å, which therefore represent the optimum QW

width for the *GaAs*-quantum-well-based lasers. Furthermore, we have found that the e-e capture process improves the carrier capture efficiency, when the carrier density in the QW is close to 10^{12}cm^{-2}. Above that density the electron capture time near the resonance minima is almost entirely governed by the e-e interaction.

Appendix A

Carrier-Carrier Interaction with Multisubband Static Screening

Let two carriers with vectors $\mathbf{r}_1$ and $\mathbf{r}_2$ interact via a Coulomb potential $V(\mathbf{r}_1-\mathbf{r}_2)$. The 3D vectors $\mathbf{r}_1$ and $\mathbf{r}_2$ can be decomposed to z components and 2D vectors $\mathbf{R}_1$ and $\mathbf{R}_2$ as $\mathbf{r}_i = (\mathbf{R}_i, z_i)$; $i = 1,2$. Using the decomposition, a Fourier transform of the potential $V(\mathbf{r}_1-\mathbf{r}_2)$ is [32]

$$V(\mathbf{Q}, z_1, z_2) = \int d\mathbf{R}\, e^{-i\mathbf{Q}\cdot\mathbf{R}} V(\mathbf{R}, z_1 - z_2), \qquad \mathbf{R} = \mathbf{R}_1 - \mathbf{R}_2.$$

The carrier with the vector $\mathbf{r}_2$ evokes the screened potential $V(\mathbf{r}_1-\mathbf{r}_2)$ in the point with the vector $\mathbf{r}_1$ which is given by the Poisson equation [48]

$$\triangle V(\mathbf{r}_1-\mathbf{r}_2) = -\frac{1}{\kappa}\left[e\,\delta(\mathbf{R}_1-\mathbf{R}_2)\,\delta(z_1-z_2) + \rho_e^{ind}(\mathbf{r}_1) + \rho_h^{ind}(\mathbf{r}_1)\right], \tag{A.1}$$

where ρ_e^{ind} and ρ_h^{ind} are the induced charge densities created after the redistribution of the electrons and holes, respectively. Charge densities of the electrons and holes are assumed to be primarily homogeneous in space. Respective induced potentials are superposed to the original Coulomb potential in the point with the vector $\mathbf{r}_2$ to create a screening of the Coulomb potential. If we assume that the screened Coulomb center does not move, then ρ_e^{ind} and ρ_h^{ind} are time-independent. It means that the screening is static. However, since the carriers move, the static screening implies that the redistribution of the carrier density in space occurs immediately [49, 50].

A.1 Screened Coulomb Potential

The Fourier transform of Eq. (A.1) is

$$\left(\frac{d^2}{dz^2} - Q^2\right) V(\mathbf{Q}, z_1, z_2) = -\frac{e}{\kappa}\,\delta(z_1-z_2) - \frac{1}{\kappa}\left[\rho_e^{ind}(\mathbf{Q}, z_1) + \rho_h^{ind}(\mathbf{Q}, z_1)\right], \tag{A.2}$$

where the Fourier transform of the induced space charge density is

$$\rho_\alpha^{ind}(\mathbf{Q}, z_1) = \int_{-\infty}^{\infty} d\mathbf{R}\, e^{-i\mathbf{Q}\cdot\mathbf{R}} \rho_\alpha^{ind}(\mathbf{R}, z_1) \quad , \qquad \alpha = e, h. \tag{A.3}$$

We take $\mathbf{R}_2 = 0$ in the Fourier transform (A.2) for simplicity. A formal solution of Eq. (A.2) for $\rho_\alpha^{ind}(\mathbf{Q}, z_1) = 0$ is a Green function $G(z_1, z_2)$, which can be found as a Fourier integral in the form

$$G(z_1, z_2) = -\frac{e}{2\pi\kappa}\int_{-\infty}^{\infty} dq\, e^{-iq(z_1-z_2)} g(q). \tag{A.4}$$

If the formal solution (A.4) and the relation

$$2\pi\delta(z_1 - z_2) = \int_{-\infty}^{\infty} dq\, e^{-iq(z_1-z_2)}$$

are substituted into Eq. (A.2) then the function $g(q) = -(q^2 + Q^2)^{-1}$. When this function is set back into Eq. (A.4) and an integration in the complex plain is performed, the Green function (A.4) is

$$G(z_1, z_2) = \frac{e}{2\kappa}\frac{1}{Q} e^{-Q|z_1-z_2|}. \tag{A.5}$$

A general solution of Eq. (A.4) has the form

$$V(\mathbf{Q}, z_1, z_2) = G(z_1, z_2) + \frac{1}{e}\int_{-\infty}^{\infty} dz'\, G(z_1, z') \left[\rho_e^{ind}(\mathbf{Q}, z') + \rho_h^{ind}(\mathbf{Q}, z')\right] + Y_0(z_1) \tag{A.6}$$

where the function Y_0 is the solution of Eq. (A.4) without the right-hand side. The function Y_0 can be chosen for physical reasons as zero. Substituting Eq. (A.5) into Eq. (A.6) the Coulomb potential is obtained as

$$V(\mathbf{Q}, z_1, z_2) = \frac{e}{2\kappa}\frac{1}{Q} e^{-Q|z_1-z_2|} + \frac{1}{2\kappa}\frac{1}{Q}\int_{-\infty}^{\infty} dz'\, e^{-Q|z_1-z_2|} \left[\rho_e^{ind}(\mathbf{Q}, z') + \rho_h^{ind}(\mathbf{Q}, z')\right]. \tag{A.7}$$

The first term on the right-hand side of Eq. (A.7) is the Fourier transform of the unscreened Coulomb center and the second one represents the screening. The next step is to find the induced space charge densities ρ_e^{ind} and ρ_h^{ind}.

We can consider a region in a sufficient distance from an electron where the potential $V(\mathbf{R}, z)$ is a slowly varying function over $\mathbf{R}$ [48, 51]. The potential energy $-eV(\mathbf{R}, z)$ can be taken as a small perturbation in the equation for the electron wave function $\phi_l^e(z)$. The perturbation does not change the electron wave function $\phi_l^e(z)$ in the first order of the perturbation theory but changes the eigenenergy ε_l by

$$\Delta\varepsilon_l(\mathbf{R}) = -e\int dz\, \phi_l^e(z) V(\mathbf{R}, z - z_2)\phi_l^e(z), \qquad l = 1, 2, \cdots, L, \tag{A.8}$$

where L is the number of electron subbands. Consequently, the sheet electron density N_l^e in the l-th subband depends on $\mathbf{R}$ and in case of the isotropic nonequilibrium distribution it can be written as

$$N_l^e(\mathbf{R}) = 2\frac{m_e}{2\pi\hbar^2}\int_0^{\infty} d\varepsilon\; f_l\left(\varepsilon + \varepsilon_l + \Delta\varepsilon_l(\mathbf{R})\right), \qquad \varepsilon = \frac{\hbar^2 k^2}{2m_e}, \tag{A.9}$$

where $f_l(\varepsilon + \varepsilon_l)$ is the nonequilibrium energy distribution in the l-th subband for $\Delta\varepsilon_l(\mathbf{R}) = 0$. If the approximation

$$f_l\left(\varepsilon + \varepsilon_l + \Delta\varepsilon_l(\mathbf{R})\right) \approx f_l(\varepsilon + \varepsilon_l) + \frac{\partial}{\partial\varepsilon} f_l(\varepsilon + \varepsilon_l)\Delta\varepsilon_l(\mathbf{R})$$

is assumed in Eq. (A.9), the expression for the sheet electron density is obtained in the form

$$N_l^e(\mathbf{R}) = N_l^e + 2\frac{m_e}{2\pi\hbar^2}\int_0^\infty d\varepsilon\,\frac{\partial}{\partial\varepsilon}\,f_l(\varepsilon+\varepsilon_l)\Delta\varepsilon_l(\mathbf{R}) = N_l^e - 2\frac{m_e}{2\pi\hbar^2}\,f_l(0+\varepsilon_l)\Delta\varepsilon_l(\mathbf{R}). \quad \text{(A.10)}$$

The induced electron charge density is given by

$$\rho_e^{ind}(\mathbf{R},z) = e\sum_n \phi_n^e\,(N_n^e - N_n^e(\mathbf{R}))\,\phi_n^e(z). \quad \text{(A.11)}$$

When Eqs. (A.8) and (A.10) are substituted into the relation (A.11) then the electron induced charge density reads

$$\rho_e^{ind}(\mathbf{R},z) = -2\frac{m_e}{2\pi\hbar^2}e^2\sum_{l=1}^{L}[\phi_l^e(z)]^2 f_l(\mathbf{k}=0)\int_{-\infty}^{\infty}dz'\,\left[\phi_l^e(z')\right]^2 V(\mathbf{R},z'-z_2) \quad \text{(A.12)}$$

where $f_n(\mathbf{k}=0)$ is the abbreviation for $f_n(0+\varepsilon_n)$. The summation over l means the summation of contributions from the electrons in all subbands to the induced charge. The Fourier transform of the induced charge density is

$$\rho_e^{ind}(\mathbf{Q},z) = -2\frac{m_e}{2\pi\hbar^2}e^2\sum_{l=1}^{L}[\phi_l^e(z)]^2 f_l(\mathbf{k}=0)\int_{-\infty}^{\infty}dz'\,\left[\phi_l^e(z')\right]^2 V(\mathbf{Q},z'-z_2). \quad \text{(A.13)}$$

The same procedure can be used for the holes. The result is the Fourier transform of the induced hole density,

$$\rho_h^{ind}(\mathbf{Q},z) = -2\frac{m_h}{2\pi\hbar^2}e^2\sum_{k=1}^{K}\left[\phi_k^h(z)\right]^2 f_k(\mathbf{k}=0)\int_{-\infty}^{\infty}dz'\,\left[\phi_k^h(z')\right]^2 V(Q,z'-z_2), \quad \text{(A.14)}$$

where K is the number of hole subbands.

A.2 Coulomb Matrix Element

Equations (A.13) and (A.14) can be substituted into Eq. (A.7) to give a final equation for the Coulomb potential [32, 51]

$$\begin{aligned} V(\mathbf{Q},z_1,z_2) = {} & \frac{e}{2\kappa Q}e^{-Q|z_1-z_2|} - \\ & - \sum_{l=1}^{L}\frac{Q_l^e}{Q}\int_{-\infty}^{\infty}dz''\,\left[\phi_l^e(z'')\right]^2 e^{-Q|z_1-z''|}\int_{-\infty}^{\infty}dz'\,\left[\phi_l^e(z')\right]^2 V(\mathbf{Q},z',z_2) - \\ & - \sum_{k=1}^{K}\frac{Q_k^h}{Q}\int_{-\infty}^{\infty}dz''\,\left[\phi_l^h(z'')\right]^2 e^{-Q|z_1-z''|}\int_{-\infty}^{\infty}dz'\,\left[\phi_l^h(z')\right]^2 V(\mathbf{Q},z',z_2). \end{aligned} \quad \text{(A.15)}$$

The first term on the right-hand side of (A.15) is the bar Coulomb interaction, the second and third terms describe the screening by electrons and holes, respectively, and

$$Q_l^e = \frac{e^2 m_e}{2\pi\kappa\hbar^2} f_l^e(\mathbf{k}=0) \quad , \qquad Q_k^h = \frac{e^2 m_h}{2\pi\kappa\hbar^2} f_k^h(\mathbf{k}=0)$$

are the 2D electron and hole screening constants in the l-th electron and k-th hole subbands, respectively.

If the Coulomb potential (A.15) is multiplied by the electron wave function ϕ_l^e for $l = 1,2,\cdots,L$ and by the hole wave function ϕ_k^h for $k = 1,2,\cdots,K$, and then integrated over z', the following two sets of mutually coupled equations are found

$$\begin{aligned}
&\left(1+A_{pp}^e\right) x_p^e + \sum_{l=1,l\neq p}^{L} C_{pl}^{ee} x_l^e + \sum_{k=1}^{K} C_{pk}^{he} x_k^h = B_p^e \quad , \qquad p = 1,2,\cdots,L, \\
&\sum_{l=1}^{L} C_{rl}^{eh} x_l^e + \left(1+A_{rr}^h\right) x_r^h + \sum_{k=1,k\neq r}^{K} C_{rk}^{hh} x_k^h = B_r^h \quad , \qquad r = 1,2,\cdots,K,
\end{aligned} \tag{A.16}$$

where

$$\begin{aligned}
x_i^\eta &= \int_{-\infty}^{\infty} dz' \left[\phi_i^\eta(z')\right]^2 V(Q,z',z_2), \\
A_{ii}^\eta &= \frac{Q_i^\eta}{Q} \int_{-\infty}^{\infty} dz' \left[\phi_i^\eta(z')\right]^2 \int_{-\infty}^{\infty} dz'' \left[\phi_i^\eta(z'')\right]^2 e^{-Q|z'-z''|}, \\
B_i^\eta &= \frac{e}{2\kappa Q} \int_{-\infty}^{\infty} dz' \left[\phi_i^\eta(z')\right]^2 e^{-Q|z'-z_2|} \quad ; \qquad \eta = e,h, \\
C_{ij}^{\eta\vartheta} &= \frac{Q_j^\eta}{Q} \int_{-\infty}^{\infty} dz' \left[\phi_i^\eta(z')\right]^2 \int_{-\infty}^{\infty} dz'' \left[\phi_j^\vartheta(z'')\right]^2 e^{-Q|z'-z''|} \quad ; \qquad \eta,\vartheta = e,h.
\end{aligned}$$

The solutions of the linear equation system (A.16) are

$$x_i = \frac{D_i}{D} \qquad \text{for} \qquad i = 1,2,\cdots,L,L+1,\cdots,L+K. \tag{A.17}$$

The determinant D in the above solutions has the form

$$D = \begin{vmatrix}
1+A_{11}^e & C_{12}^{ee} & \cdots & C_{1L}^{ee} & C_{11}^{he} & C_{12}^{he} & \cdots & C_{1K}^{he} \\
C_{21}^{ee} & 1+A_{22}^e & \cdots & C_{2L}^{ee} & C_{21}^{he} & C_{22}^{he} & \cdots & C_{2K}^{he} \\
\vdots & \vdots & & \vdots & \vdots & \vdots & & \vdots \\
C_{L1}^{ee} & C_{L2}^{ee} & \cdots & 1+A_{LL}^e & C_{L1}^{he} & C_{L2}^{he} & \cdots & C_{LK}^{he} \\
C_{11}^{eh} & C_{12}^{eh} & \cdots & C_{1L}^{eh} & 1+A_{11}^h & C_{12}^{hh} & \cdots & C_{1K}^{hh} \\
\vdots & \vdots & & \vdots & \vdots & \vdots & & \vdots \\
C_{K1}^{eh} & C_{K2}^{eh} & \cdots & C_{KL}^{eh} & C_{K1}^{hh} & C_{K2}^{hh} & \cdots & 1+A_{KK}^h
\end{vmatrix}.$$

The determinants D_i arise from the determinant D when the i-column of D is replaced with the right-hand side of (A.16) so that

$$D_i = \begin{vmatrix} 1+A^e_{11} & C^{ee}_{12} & \cdots & C^{ee}_{1i-1} & B^e_1 & C^{ee}_{1i+1} & \cdots & C^{ee}_{1L} & C^{he}_{11} & \cdots & C^{he}_{1K} \\ C^{ee}_{21} & 1+A^e_{22} & \cdots & C^{ee}_{2i-1} & B^e_2 & C^{ee}_{2i+1} & \cdots & C^{ee}_{2L} & C^{he}_{21} & \cdots & C^{he}_{2K} \\ \vdots & \vdots & & \vdots & \vdots & \vdots & & \vdots & \vdots & & \vdots \\ C^{ee}_{L1} & C^{ee}_{L2} & \cdots & C^{ee}_{Li-1} & B^e_L & C^{ee}_{Li+1} & \cdots & 1+A^e_{LL} & C^{he}_{L1} & \cdots & C^{he}_{LK} \\ C^{eh}_{11} & C^{eh}_{12} & \cdots & C^{eh}_{1i-1} & B^h_1 & C^{eh}_{1i+1} & \cdots & C^{eh}_{1L} & 1+A^h_{11} & \cdots & C^{hh}_{1K} \\ \vdots & \vdots & & \vdots & \vdots & \vdots & & \vdots & \vdots & & \vdots \\ C^{eh}_{K1} & C^{eh}_{K2} & \cdots & C^{eh}_{Ki-1} & B^h_K & C^{eh}_{1K+1} & \cdots & C^{eh}_{KL} & C^{hh}_{K1} & \cdots & 1+A^h_{KK} \end{vmatrix} .$$

The solutions (A.17) can be substituted into Eq. (A.15) to express the Coulomb potential as

$$V(\mathbf{Q},z_1,z_2) = \frac{e}{2\kappa Q}e^{-Q|z_1-z_2|} - \sum_{l=1}^{L}\frac{Q^e_l}{Q}\int_{-\infty}^{\infty}dz''\,\left[\phi^e_l(z'')\right]^2 e^{-Q|z_1-z''|}\frac{D_l(z_2)}{1+\sum_{s=1}^{(L+K)!-1}O_s} - \\ - \sum_{k=1}^{K}\frac{Q^h_k}{Q}\int_{-\infty}^{\infty}dz''\,\left[\phi^h_k(z'')\right]^2 e^{-Q|z_1-z''|}\frac{D_{k+L}(z_2)}{1+\sum_{s=1}^{(L+K)!-1}O_s}, \quad \text{(A.18)}$$

where O_s are terms not equal to the unity term. It means that the unity term always appears in the determinant D. It is in an agreement with the well-known form of the static screening function. The Coulomb matrix element

$$\int_{-\infty}^{\infty}dz_1\int_{-\infty}^{\infty}dz_2\,\phi_i(z_1)\phi_j(z_2)V(\mathbf{Q},z_1,z_2)\phi_m(z_1)\phi_n(z_2) \quad \text{(A.19)}$$

is then easy to evaluate.

The e-h scattering rate (4.3) and the e-e scattering rate (4.7) are obtained using the Coulomb matrix element (A.19) for $L=K=1$ and for $L=1,K=0$, respectively. Taking $K=0$ in the e-e interaction we neglect the screening by the holes. This corresponds to a so-called quasi-dynamic approximation [36], in which heavy holes are not able to follow fast changes of electron positions. Finally, as in the previous papers [18, 41], we restrict ourselves to the screening by quasi-equilibrium carriers in the QW. In our conditions (the density of the carriers equal to $10^{11}cm^{-2}$ or $10^{12}cm^{-2}$, the lattice temperature 8 K) the quasi-equilibrium carriers occupy mainly the lowest subband of the QW. Therefore, we neglect L and K greater than 1.

List of Symbols

A	Normalization area
b	Barrier width
D	Diffusion constant
D_0	Non-polar deformation potential
e	Electron charge
E	Energy
f_i^e	Electron distribution function in the subband i
f_j^h	Hole distribution function in the subband j
F	Fermi energy, Form factor
$\hbar$	Dirac constant or Planck constant over 2π
$\mathbf{k}$	Carrier wavevector
k_B	Boltzmann constant
ℓ	Mean free path of the hole
m_e	Electron effective mass in the quantum well
m_h	Hole effective mass in the quantum well
m_e^B	Electron effective mass in the barrier
m_h^B	Hole effective mass in the barrier
n	Carrier density in the barrier
N, N_S	Carrier sheet density in the quantum well
$\mathbf{r}, \mathbf{R}$	Carrier real-space vector
T	Temperature
$T_{A\to B}$	Transmission coefficient from A to B
t	Time
v_h^W	Hole velocity in the quantum well
V	Coulomb potential
V_w	Potential difference in the conduction band between the quantum well and barrier
V_w^h	Potential difference in the valence band between the quantum well and barrier
V_b	Potential difference in the conduction band between the barrier and cladding layer
w	Quantum well width
ε	Energy

κ	Static permittivity in the quantum well
κ^B	Static permittivity in the barrier
κ_∞	High-frequency permittivity in the quantum well
θ	Angle
λ	Wavelenght, Scattering rate
ν	Frequency
ρ_e^{ind}	Electron space charge
ρ_h^{ind}	Hole space charge
τ	Relaxation time, Capture time
ϕ	Angle
χ_i^e	Electron wavefunction in the subband i
χ_j^h	Hole wavefunction in the subband j
ω_0	Frequency of non-polar optical phonons
ω_{LO}	Frequency of longitudinal optical phonons

Bibliography

[1] M J Kelly: *Low-Dimensional Semiconductors* (Clarendon Press, Oxford, 1995) p 422.

[2] O Svetlo: *Principles of Lasers* (3rd ed., Plenum Press, New York, 1989) p 254.

[3] M Ali Omar: *Elementary Solid State Physics* (Addison-Wesley, Reading, 1975) p 349.

[4] M G A Bernard and G Duraffourg: *Phys. Status Solidi* **1** (1961) 699.

[5] Ben G Streetman: *Solid State Electronic Devices* (Prentice-Hall, 2nd ed., New Jersey, 1980) p 389.

[6] S M Sze: *Physics of Semiconductor Devices* (J. Wiley & Sons, 2nd ed., N. Y., 1981) p 255; H A Bethe: *MIT Radiat. Lab. Rep.* **42-12** (1942).

[7] P K Tien: *Rev. Mod. Phys.* **49** (1977) 361.

[8] C Weisbuch and J Nagle: in *Science and Engineering of One- and Zero-Dimensional Semiconductors* ed. by S P Beaumont and C M Sotomayor Torres (NATO ASI Series, Plenum Press, New York, 1990) p 309.

[9] C W Corzine, R-H Yan, and L A Coldren: in *Quantum Well Lasers* ed. by P S Zorry, Jr. (Academic Press, San Diego, 1993) p 32.

[10] W W Chow, S W Koch, and M Sargent III: *Semiconductor-Laser Physics* (Springer-Verlag, Heidelberg, 1994) p 14.

[11] P W M Blom, C Smit, J E M Haverkort, and J H Wolter: *Phys. Rev.* B **47** (1993) 2072.

[12] P W M Blom: *Carrier Capture in III-V Semiconductor Quantum Wells*, PhD thesis (Technical University of Eindhoven, 1992).

[13] J Shah: *Ultrafast Spectroscopy of Semiconductors and Semiconductor Nanostructures* (Springer-Verlag, Berlin, 1996) p 316.

[14] H Mahr and M D Hirsch: *Opt. Commun.* **13** (1975) 96.

[15] M R X Barros, P C Becker, S D Morris, B Deveaud, A Regreny, and F Beisser: *Phys. Rev.* B **47** (1993) 10 951.

[16] J A Brum and G Bastard: *Phys. Rev.* B **33**, (1986) 1420.

[17] S V Kozyrev and A Ya Shik: *Fiz. Tech. Poluprovodn.* **19**, 1667 (1985) [*Sov. Phys. Semicond.* **19**, 1024 (1985)].

[18] P W M Blom, J E M Haverkort, P J van Hall, and J H Wolter: *Appl. Phys. Lett.* **62** (1993) 1490.

[19] J E M Haverkort, P W M Blom, P J Van Hall, J Claes, and J H Wolter: *Phys. Status Solidi* B **188**, (1995) 139.

[20] K Kálna, M Moško, and F M Peeters: *Appl. Phys. Lett.* **68** (1996) 117.

[21] K Kálna and M Moško: *Phys. Rev.* B **54** (1996) 17 730.

[22] L F Register, U Ravaioli, and K Hess: *J. Appl. Phys* **69** (1991) 7153; *ibid.* **71** (1992) 1555(E).

[23] L F Register and K Hess: *Phys. Rev.* B **49** (1994) 1900.

[24] L F Register and K Hess: *Superlatt. Microstruct.* **18** (1995) 223.

[25] D McDonald and R F O'Dowd: *IEEE J. Quantum Electron.* **31** (1995) 1927.

[26] K Hess, H Morkoç, H Shichijo, and B G Streetman: *Appl. Phys. Lett.* **35** (1979) 469.

[27] B R Nag: *Electron Transport in Compound Semiconductors* (Springer-Verlag, Heidelberg, 1980) p 119.

[28] C Jacoboni and L Regiani: *Rev. Mod. Phys.* **55** (1983) 645.

[29] H G Reik and H Risken: *Phys. Rev.* **124** (1961) 777.

[30] L D Landau and E M Lifshitz: *Quantum Mechanics, Non-Relativistic Theory* (Pergamon Press, 3rd ed., London, 1958) p 76.

[31] S M Goodnick and P Lugli: in *Hot Carriers in Semiconductor Nanostructures*, edited by J Shah (Academic Press, New York, 1992), p 191.

[32] A Mošková: *Elektrón-elektrónový rozptyl 2D elektrónového plynu v polovodičových kvantových jamách: Monte Carlo simulácia*, PhD thesis (Comenius University, Bratislava, 1992).

[33] Ľ Hrivnák: *Appl. Phys. Lett.* **56** (1990) 2425.

[34] R Dingle, W Wiegmann, and C H Henry: *Phys. Rev. Lett.* **33** (1974) 827.

[35] C Weisbuch and B Vinter: *Quantum Semiconductor Structures: Fundamentals and Applications* (Academic Press, Boston, 1991) p 59.

[36] M Moško, A Mošková, and V Cambel: *Phys. Rev.* B **51**, (1995) 16 860.

[37] A Mošková and M Moško: *Phys. Rev.* B **49** (1994) 7443.

[38] S M Goodnick and P Lugli: *Appl. Phys. Lett.* **51** (1987) 584.

[39] M Artaki and K Hess: *Phys. Rev.* B **37** (1988) 2933.

[40] M Moško and A Mošková: *Phys. Rev.* B **44** (1991) 10 794.

[41] P Sotirelis and K Hess: *Phys. Rev.* B **49** (1994) 7543.

[42] P Sotirelis, P von Allmen, and K Hess: *Phys. Rev.* B **47** (1993) 12 744.

[43] D W Snoke, W W Rühle, Y-C Lu, and E Bauser: *Phys. Rev. Lett.* **68** (1992) 990.

[44] M Preisel, J Mørk, and H Haug: *Phys. Rev.* B **49** (1994) 14 478.

[45] S Adachi: *J. Appl. Phys.* **58** (1985) R1.

[46] K Hess: *Advanced Theory of Semiconductor Devices* (Prentice Hall, New Jersey, 1988) p. 98.

[47] U Hohenester, P Supancic, P Kocevar, X Q Zhou, W Kütt, and H Kurz: *Phys. Rev.* B **47** (1993) 13 233.

[48] F Stern and W E Howard: *Phys. Rev.* **163** (1967) 816.

[49] T Ando, A B Fowler, and F Stern: *Rev. Mod. Phys.* **54** (1982) 437.

[50] E D Siggia and P C Kwok: *Phys. Rev.* B **2** (1970) 1024.

[51] K Yokoyama and K Hess: *Phys. Rev.* B **33** (1986) 5595.